

Electric-field-induced second-harmonic generation

Hangkai Fan, Alexey Proskurin, Mingzhao Song* and Andrey Bogdanov*

Citation: Fan HK, Proskurin A, Song MZ, Bogdanov A. Electric-field-induced second-harmonic generation. *Opto-Electron Adv* **9**, 250193(2026).

<https://doi.org/10.29026/oea.2026.250193>

Received: 28 July 2025; Accepted: 16 November 2025; Published online: 27 January 2026

Related articles

Resonantly enhanced second- and third-harmonic generation in dielectric nonlinear metasurfaces

Ji Tong Wang, Pavel Tonkaev, Kirill Koshelev et al

Opto-Electronic Advances 2024, 7(5): 230186 doi: [10.29026/oea.2024.230186](https://doi.org/10.29026/oea.2024.230186)

Sequential harmonic spin-orbit angular momentum generation in nonlinear optical crystals

Yutao Tang, Zixian Hu, Junhong Deng et al

Opto-Electronic Advances 2024, 7(12): 240138 doi: [10.29026/oea.2024.240138](https://doi.org/10.29026/oea.2024.240138)

More related articles in Opto-Electronic Journals Group website



<https://www.oejournal.org>



 OE_Journal



 @OptoElectronAdv

Electric-field-induced second-harmonic generation

Hangkai Fan^{1,2,3,4}, Alexey Proskurin⁴, Mingzhao Song^{1,2,5*} and Andrey Bogdanov^{1,4*}

Abstract: Second-harmonic generation (SHG) is a fundamental nonlinear optical process widely used in photonics; however, it is strictly forbidden in the bulk of centrosymmetric materials due to their inversion symmetry. Nevertheless, applying an external electric field breaks this inversion symmetry. It induces an effective second-order nonlinear response known as the electric-field-induced second-harmonic generation (EFISH) effect. This mechanism enables SHG in centrosymmetric media and provides a effective mechanism for electrically tunable nonlinear nanophotonics. Here, we present a comprehensive overview of the EFISH effect, covering the fundamentals, various material platforms (including bulk semiconductor crystals, ferroelectrics, van der Waals materials, and polymers), as well as diverse strategies for electric field engineering. We distinguish EFISH from related effects including current-induced SHG and the quantum-confined Stark effect, and highlight emerging applications of EFISH in tunable photonic devices, carrier dynamics probing, and nonlinear optical modulation across optical, electronic, and THz regimes. Finally, we outline key challenges and prospects for the future development of electrically controlled nonlinear optical systems.

Keywords: EFISH; metasurface; microresonator; vdW materials; nonlinear nanophotonics; CPE

DOI: [10.29026/oea.2026.250193](https://doi.org/10.29026/oea.2026.250193) | CSTR: [32247.14.oea.2026.250193](https://cstr.org/cstr/32247.14.oea.2026.250193)

Citation: Fan HK, Proskurin A, Song MZ et al. Electric-field-induced second-harmonic generation. *Opto-Electron Adv* **9**, 250193 (2026).

1 Introduction

Second-harmonic generation (SHG) is a fundamental second-order nonlinear optical process that coherently doubles the frequency of incident light¹. The pioneering experimental demonstration by Franken et al. in 1961² and the subsequent theoretical framework developed by Bloembergen et al.^{3,4} established SHG as one of the cornerstones of modern optical technologies, including imaging, sensing, and quantum communication⁵⁻⁷. The mechanism behind SHG is the existence of second-order nonlinear polarization, expressed as $\mathbf{P}_{2\omega} = \chi^{(2)} : \mathbf{E}_\omega \otimes \mathbf{E}_\omega$ in the frequency domain, where $\chi^{(2)}$ is the tensor of third-rank intrinsically linked to the symmetry properties of the medium¹, and \mathbf{E}_ω represents the electric field at the fundamental frequency ω .

However, most reported SHG have been restricted to a limited set of non-centrosymmetric materials, such as lithium niobate (LiNbO₃)⁸ and gallium arsenide phosphide

(GaAs_{1-x}P_x)⁹, which naturally possess large bulk $\chi^{(2)} \sim 30-70$ pm/V^{10,11}. In contrast, common materials such as silicon (Si) and silicon nitride (Si₃N₄), which are compatible with complementary metal oxide semiconductor (CMOS) fabrication technology, are centrosymmetric and, thus, inherently forbid the existence of bulk $\chi^{(2)}$, suppressing SHG.

Several strategies have been developed to enable SHG in centrosymmetric materials. One approach exploits surface contributions¹², where the inversion symmetry is naturally broken at interfaces of different materials permits SHG. However, this effect is confined to only a few atomic layers, resulting in limited conversion efficiency. Alternatively, bulk inversion symmetry can be broken by applying external inhomogeneous stress to induce lattice deformation, thereby generating a strain-induced second-order susceptibility up to 40 pm/V¹³⁻¹⁶.

Another efficient method involves applying an

Received: 28 July 2025

Accepted: 16 November 2025

Published online: 27 January 2026

¹Qingdao Innovation and Development Center, Harbin Engineering University, Qingdao 266000, China; ²Key Laboratory of Photonic Materials and Device Physics for Oceanic Applications, Ministry of Industry and Information Technology of China, Harbin 150001, China; ³College of Information and Communication Engineering, Harbin Engineering University, Harbin 150001, China; ⁴School of Physics and Engineering, ITMO University, St. Petersburg 191002, Russia; ⁵College of Physics and Optoelectronic Engineering, Harbin Engineering University, Harbin 150001, China.

*Correspondence: MZ Song, E-mail: kevinsmz@foxmail.com; A Bogdanov, E-mail: bogdan.taurus@gmail.com

electrostatic field in the bulk material. This electrostatic field perturbs the electronic potential without altering the crystallographic lattice structure and induces an effective second-order nonlinearity given by $\chi_{\text{eff}}^{(2)} = 3\chi^{(3)} : E_{\text{DC}}$ ^{4,17}, named electric-field-induced second-harmonic generation (EFISH). This effect not only enables SHG in bulk centrosymmetric materials, but also provides a promising pathway to dynamic and reversible control of SHG through electrical modulation. By analogy, the Kerr effect modulates the effective linear susceptibility as $\delta\chi_{\text{eff}}^{(1)} \propto \chi^{(3)} : (E_{\text{DC}} \otimes E_{\text{DC}})$ ^{18,19}, whereas EFISH modulates the effective second-order susceptibility $\delta\chi_{\text{eff}}^{(2)} \propto \chi^{(3)} : E_{\text{DC}}$ ²⁰. This electrically programmable $\chi_{\text{eff}}^{(2)}$ characteristic provides a promising approach for the development of electrically tunable nonlinear optical devices⁷.

EFISH is often conflated with the similar effects such as current-induced SHG (CISH)²¹ and the quantum-confined stark effect (QCSE)^{22–26}. All these effects enable electrical tuning of the effective second-order susceptibility. However, their underlying physical mechanisms differ significantly.

In this work, we provide a comprehensive overview of recent advances in EFISH. Section 2 introduces the theoretical foundations of EFISH, CISH, and QCSE, clarifying their differences and providing the foundation for subsequent discussions. Recent progress in EFISH is reviewed in three key areas: 1) nonlinear material selection, including bulk centrosymmetric crystals, ferroelectric materials, van der Waals (vdW) materials, and organic polymers; 2) electrostatic fields engineering, covering both externally applied

and optically generated fields; 3) photonic mode design, exploring EFISH enhancement through resonance in metallic and dielectric metasurfaces. Section 3 provides a brief review of CISH and QCSE to highlight their distinct physical platform and performance differences. Section 4 addresses practical applications of EFISH, particularly in optical manipulation and carrier dynamics probing. Finally, we provide a comprehensive discussion on current challenges and promising future research directions. The key topics reviewed in this article are summarized in Fig. 1.

2 Fundamentals and recent progress on EFISH

When a photon impinges on a material, electrons are displaced from equilibrium, forming oscillating electric multipoles (e.g., dipole, quadrupole and higher orders). These multipoles radiate and modify the local field, giving rise to various optical phenomena including reflection, transmission, and harmonic generation. Collectively, these induced multipoles constitute the polarization \mathbf{P} which can be expanded as:

$$\mathbf{P} = \chi^{(1)} : \mathbf{E} + \chi^{(2)} : (\mathbf{E} \otimes \mathbf{E}) + \chi^{(3)} : (\mathbf{E} \otimes \mathbf{E} \otimes \mathbf{E}) + \dots, \quad (1)$$

where $\chi^{(N)}$ is an $(N + 1)$ st-rank tensor of N th-order nonlinear susceptibility, characterizing the intrinsic material property to generate N th-order harmonic (e.g., $\chi^{(2)}$ is a third-

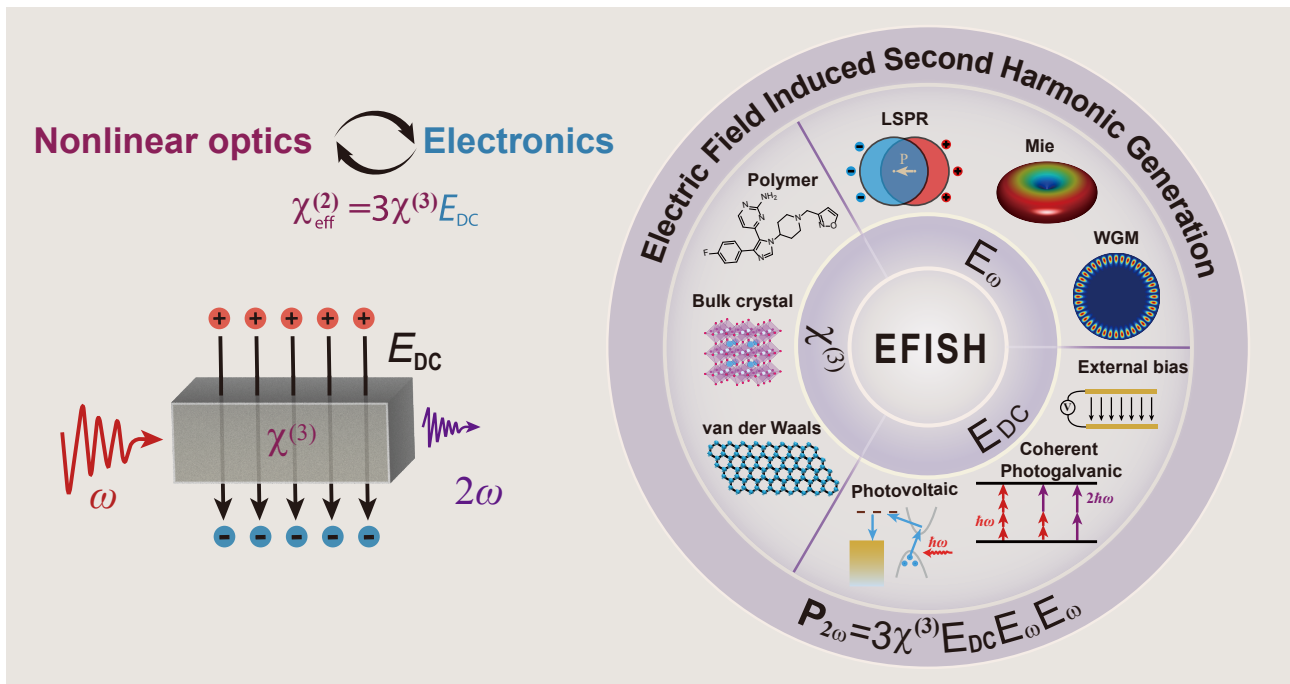


Fig. 1 | Schematic overview of the key topics covered in this review. The EFISH effect emerges from the intimate coupling between electronic dynamics and nonlinear photonic. Depending on the EFISH functionality, the research can be categorized in to three topics: (i) nonlinear material engineering; (ii) electrostatic field engineering; (iii) fundamental electric field engineering.

rank tensor governing SHG)¹.

Generally, the components of the $(N + 1)$ th-order nonlinear susceptibility tensor $\chi_{i_1 \dots i_{N+1}}^{(N+1)}$ are typically 8–10 orders of magnitude smaller than those of $\chi_{i_1 \dots i_N}^{(N)}$. At moderate field amplitude, nonlinear contribution to the polarization is negligible, and the total polarization remains essentially synchronous with the incident field, allowing only for linear optical phenomena. When the field amplitude becomes sufficiently large, the second-order nonlinear polarization: $\mathbf{P}_{2\omega, NL} = \chi^{(2)}(\omega, \omega) : \mathbf{E}_\omega \otimes \mathbf{E}_\omega$ emerges and gives rise to SHG, wherein two photons of energy $\hbar\omega$ coherently combine to produce one photon of energy $\hbar 2\omega$. The SH photon in turn induces a linear polarization $\mathbf{P}_{2\omega, L} = \chi^{(1)}(2\omega) : \mathbf{E}_{2\omega}$. These linear and nonlinear polarization contributions at 2ω interfere coherently. Consequently, an efficient SHG output requires phase matching and mode matching as illustrated in Fig. 2(a). Equivalently, SHG is a coherent two-photon process that conserves energy and the relevant quantum numbers specified by the photonic potential (e.g., spatial symmetry of the refractive index $n(\mathbf{r})$).

Specifically, in the systems with translational symmetry (e.g. homogeneous media or a waveguide), photonic modes propagate and are characterized by a linear momentum quantum number. The SHG process requires the linear momentum conservation (phase matching)¹:

$$\Delta \mathbf{k} = 2\mathbf{k}(\omega) - \mathbf{k}(2\omega) = 0. \quad (2)$$

In the systems lacking translational symmetry (e.g., a single dielectric resonator), momentum will not be the quantum number for the photonic eigenmodes. The relevant selection rules come from the remaining symmetries. In this case, the conversion of these quantum numbers (mode matching) κ_{12} becomes critical, which is macroscopically characterized by the spatial and spectral overlap between relevant modes^{27–31}:

$$\kappa_{12} = \underbrace{\left| \frac{\text{Im} \{ \tilde{\omega}_{SH} \}}{\text{Re} \{ 2\tilde{\omega}_{FH} \} - \tilde{\omega}_{SH}} \right|^2}_{\text{spectral overlap}} \times \underbrace{\int_V \mathbf{E}_{SH} \cdot [\chi^{(2)} : (\mathbf{E}_{FH} \otimes \mathbf{E}_{FH})] d^3 \mathbf{r}}_{\text{spatial overlap}}, \quad (3)$$

where $\tilde{\omega}_{FH}$ and $\tilde{\omega}_{SH}$ represent the complex eigenfrequency of the fundamental harmonic (FH) and SH mode, respectively, as shown in Fig. 2(b). We should note that this spatial overlap can vanish even in non-centrosymmetric materials ($\chi^{(2)} \neq 0$) due to symmetry constraints of the mode profile. Therefore, the selection rules for nonlinear conversion are defined by both the spatial symmetry of photonic modes and the orientation of the nonlinear susceptibility tensor³². For deep subwavelength structures, such as atomically thin two-dimensional materials, quantum dots, or quantum wells, a variety of quantum effects predominantly govern SHG³³.

In the dipole approximation, the second-order nonlinear susceptibility $\chi^{(2)}$ (with SI units mV^{-1}) originates from the asymmetry term of the electronic potential energy³⁴, which is highly sensitive to inversion symmetry of materials. In centrosymmetric materials, inversion symmetry implies the opposite SH electron responses at $\pm \mathbf{k}$ wavevectors, which cancel second-harmonic contributions across the material. Equivalently, the electron potential is even in real space under inversion symmetry so that the electron oscillation is symmetric which do not contribute to the second-order harmonic, as depicted in Fig. 3(a). In mathematical terms, the bulk nonlinear polarization under inversion symmetry follows the condition:

$$\mathbf{P}_{2\omega} = \chi^{(2)}(-\mathbf{r}) : [(-\mathbf{E}_\omega) \otimes (-\mathbf{E}_\omega)] = -\mathbf{P}_{2\omega}, \quad (4)$$

necessitating $\chi^{(2)}(-\mathbf{r}) = -\chi^{(2)}(\mathbf{r})$, which implies $\chi^{(2)} = 0$. Thus, natural SHG inherently occurs only in non-

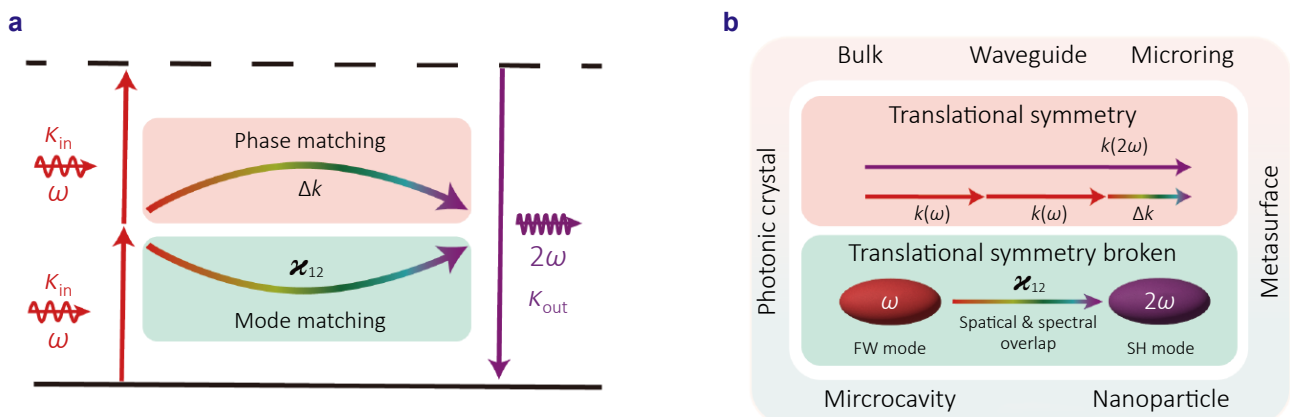


Fig. 2 | Fundamentals of SHG. (a) Schematic energy-level diagram illustrating SHG. Efficient nonlinear harmonic generation requires both phase matching and mode matching. (b) Illustration of phase versus mode matching based on translational symmetry. In systems with preserved translational symmetry (e.g., bulk media, waveguides and microring), momentum is a well-defined quantum number and phase matching is essential. When translational symmetry is broken (e.g., unitcell of metasurfaces²⁷, photonic crystals defect cavities²⁹, and nanoparticle²⁸), phase matching is relaxed and mode matching governs this nonlinear process.

centrosymmetric materials³⁵. However, applying an electrostatic field E_{DC} in centrosymmetric materials distorts the electron cloud, preventing the complete cancellation of SH polarization and rendering the asymmetric potential energy, as illustrated in Fig. 3(b) and Fig. 3(c).

It is important to clearly distinguish EFISH from similar effects such as CISH³⁶ and QCSE²⁶, all of which can electrically modulate the $\chi_{eff}^{(2)}$. While CISH also breaks centrosymmetry through current bias, its underlying symmetry-breaking mechanism is fundamentally different.

In detail, EFISH arises from the asymmetric electron potential induced by an external electrostatic field. In materials with a high carrier density, however, Debye screening strongly suppresses the internal electrostatic field, rendering EFISH ineffective. In such cases, symmetry is broken by an applied electric current, leading to CISH. This effect originates from a tilted Fermi level that breaks the symmetry of electron distribution in the momentum space. This nonequilibrium electron population prevents complete cancellation of the SHG contributions, see Fig. 3(d). Consequently, an effective $\chi_{eff}^{(2)}$ is induced and acquires helicity and polarity set by the current direction.

Another effect, QCSE, predominates in non-centrosymmetric low-dimensional systems such as vdW materials²⁴ and quantum-engineered heterostructures²². In these systems, quantum confinement creates excitons, quasiparti-

cles comprising Coulomb-bound electron-hole pairs and intersubband transitions (ISTs). Both excitonic and IST features appear as sharp resonances in the second-order nonlinear susceptibility spectrum, determined by the electronic bandgap³⁷. An electric field applied along the confinement direction tilts the electronic potential and redistributes electron-hole wavefunctions, producing a Stark shift. Consequently, QCSE enables electrical control of the spectral position and magnitude of these resonances as illustrated in Fig. 3(f, g).

In general, EFISH can be expressed as³⁸:

$$P_{2\omega} = (\chi^{(2)} + \underbrace{3\chi^{(3)} : E_{DC}}_{\chi_{eff}^{(2)} \propto E_{DC}}) : E_{\omega} \otimes E_{\omega}, \quad (5)$$

where $\chi^{(2)}$ and $\chi^{(3)}$ are the intrinsic second- and third-order nonlinear susceptibilities, E_{DC} is the external field slowly varying in time compared to the optical wave oscillation period, and $3\chi^{(3)} : E_{DC}$ term is the effective second-order susceptibility induced by the EFISH effect. In non-centrosymmetric materials, however, $\chi^{(3)}$ is typically much smaller than $\chi^{(2)}$, and therefore, EFISH is negligible compared to intrinsic SHG. Thus, EFISH studies predominantly focus on centrosymmetric materials ($\chi^{(2)} = 0$), where SH signals originate solely from EFISH, enabling significant modulation depths. EFISH research primarily addresses three key aspects derived from Eq. (5): (i) $\chi^{(3)}$: selecting

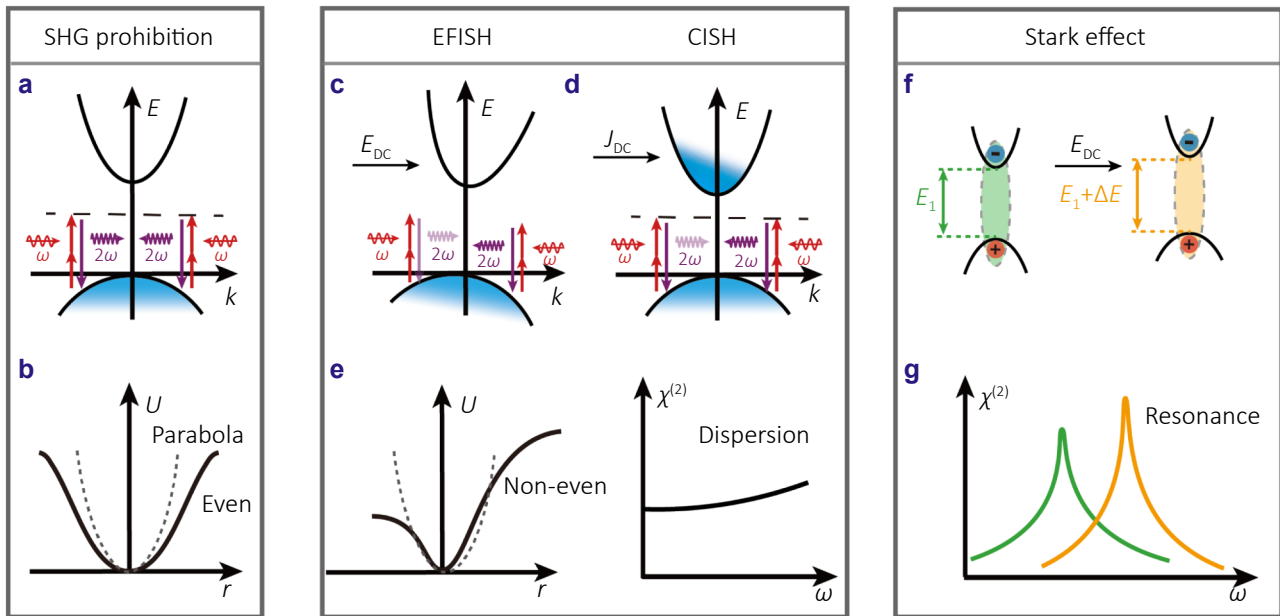


Fig. 3 | Distinct mechanisms of EFISH, CISH, and QCSE. (a, b) In centrosymmetric materials, symmetric electron distribution in momentum space (blue area), corresponding to an even potentials in real space, leads to mutually cancelling second-harmonic polarization, thereby forbidding SHG. (c) Application of an external electric field breaks centrosymmetry by inducing asymmetric electron potentials between momentum states at $\pm k$ (EFISH). (d) In the material with high carrier density, electrostatic field is screened and carriers movement (current) breaks symmetry through asymmetric electron distributions in momentum space (CISH). (e) Both EFISH and CISH broken the inversion symmetry enabling non-even potential function giving rise to effective second-order nonlinear susceptibility $\chi_{eff}^{(2)}$ with dispersion. (f, g) Formation of excitons or IST leads to resonant enhancement in $\chi_{eff}^{(2)}$. Application of an electrostatic field modifies the electronic band structure via the stark effect, thereby modulating this resonant $\chi_{eff}^{(2)}$.

nonlinear optical materials, (ii) E_{DC} : engineering electrostatic field, and (iii) E_{ω} : manipulating electric field at the pump frequency. Specifically, both (i) and (ii) involve material properties, (i) emphasizes intrinsic nonlinear optical characteristics, whereas (ii) highlights semiconductor electrical properties. Moreover, aspects (ii) and (iii) involve structural considerations: aspect (ii) addresses electrical structure designs (e.g., metal-semiconductor-metal or p-i-n junctions), whereas aspect (iii) emphasizes engineered photonic structures, such as metasurfaces, and single resonators.

2.1 Selection of nonlinear optical materials

Nonlinear optical materials used in EFISH can be organized into three categories — bulk crystals, organic polymers, and quantum-wells-based materials — based on their electron-photon interaction model. In bulk crystals, electrons evolve in a periodic potential, so the band structure governs their response³⁹. The crystal point-group symmetry imposes strict constraints on the allowed components of nonlinear susceptibility tensors. In organic polymers, molecular hyperpolarizabilities underpin optical response, which originates from the π -conjugated electron delocalization and donor-acceptor charge transfer⁴⁰. However, in unoriented polymer films, the macroscopic second-order response is averaged to zero due to random molecular orientations. In vdW crystals, electron dynamics evolve within an effectively two-dimensional periodic potential, so the in-plane symmetry dictates the allowed components of the nonlinear susceptibility tensor. Specially, the number of layers and stacking order in vdW materials can modify the in-plane symmetry, thereby substantially affecting the nonlinear response⁴¹.

2.1.1 Bulk crystals

Crystal structures can be classified into 32 crystal classes, 11 of which possess centrosymmetry³⁹. For example, calcite (CaCO_3), the first material in which the EFISH signal was observed by Terhune et al.¹⁷, belongs to the centrosymmetric group D_{3d} . The measured SHG intensity exhibits a parabolic dependence on the applied external voltage, providing unambiguous evidence for the EFISH mechanism $\mathbf{P}_{2\omega} = 3\chi^{(3)} : \mathbf{E}_{DC} : \mathbf{E}_{\omega} \otimes \mathbf{E}_{\omega}$.

Beyond conventional centrosymmetric crystals, there are materials exhibiting unique electron polarization behaviors such as topological states⁴² and ferroelectric properties⁴³, which display a peculiar response to the external field. In materials with ferroelectric properties, domains possess two polarization states in the absence of an external electric field^{44,45}. These polarization states can be switched by applying an external electric field, producing a characteristic hysteresis loop⁴⁶. Correspondingly, the polarization exhibits a butterfly-shaped loop as a function of the applied field, providing a platform for electrically tunable optical devices^{47–50}.

Ferroelectrics are intrinsically non-centrosymmetric crystals, however, the SHG modulation under applied field contains contributions from both ferroelectric property and EFISH effect. To disentangle these mechanisms, Gilles et al.⁵¹ studied electrically tunable SHG in lead zirconate titanate (PZT) thin films, Fig. 4(a). The SH power has different dependencies on the applied field in low- and high-voltage regimes, where different mechanisms dominate, as illustrated in Fig. 4(b). At small absolute voltages, SHG intensity has a parabolic dependence on the voltage, which is consistent with EFISH. At large absolute voltages, the response becomes linear, attributed to the reconfiguration of ferroelectric domains.

In addition to uniform spontaneous polarization, ferroelectric systems exhibit polar skyrmions, which are non-trivial, topologically protected configurations of polarization, analogous to vortex-like domain walls with centrosymmetric characteristics^{52–55}. This phenomenon was discovered in many systems such as $\text{PbTiO}_3/\text{SrTiO}_3$ superlattices^{56–61}, where polarization forms a nanoscale periodic unit with swirling electric dipoles and long-range in-plane ordering. In situ studies of the polarization evolution in these structures reveal their strong responsiveness to external stimuli, resulting in significant changes in the polarization magnitudes. Additionally, in this ground state, skyrmions are $\chi^{(2)}$ inactive due to the pseudo-centrosymmetry of the dipoles within each skyrmion and the surrounding interfacial c domain region. These findings highlight the potential of topological polar structures for EFISH with giant modulation depths. Recently, Sixu et al.⁶² observed a giant SHG response ($\chi_{\text{eff},zzz}^{(2)} = -54.2 \text{ pm/V}$) in polar skyrmions through the EFISH effect in $\text{PbTiO}_3/\text{SrTiO}_3$ superlattice with -14 V bias as illustrated in Fig. 4(c, d). The pseudo-centrosymmetry is dramatically broken by an applied electric bias in the $\text{SrRuO}_3/\text{superlattice}/\text{SrRuO}_3$ capacitor, enabling a high-modulation depth up to $664\% \text{ V}^{-1}$.

2.1.2 Van der Waals materials

Van der Waals (vdW) layered materials are crystals composed of crystalline sheets held together by strong in-plane covalent bonds and weak out-of-plane vdW interactions^{33,63,64}. This weak interlayer force facilitates mechanical exfoliation of the materials into two-dimensional (2D) monolayers and few-layer crystals. The symmetry of few-layer 2D materials varies with the number of layers⁶⁵, influencing the nonlinear susceptibility tensor. Moreover, layered 2D materials can be synthesized with arbitrary interlayer twist angles^{66,67}, where layers remain bound by vdW interactions while preserving their individual crystal symmetries and forming moiré superlattices. This twisted stacking of 2D materials with moiré superlattices features twist angle-dependent crystal symmetry and allows exploring special Moiré exciton resonances in artificial twisted homotrilayers and heterobilayers in artificial twisted homo- and

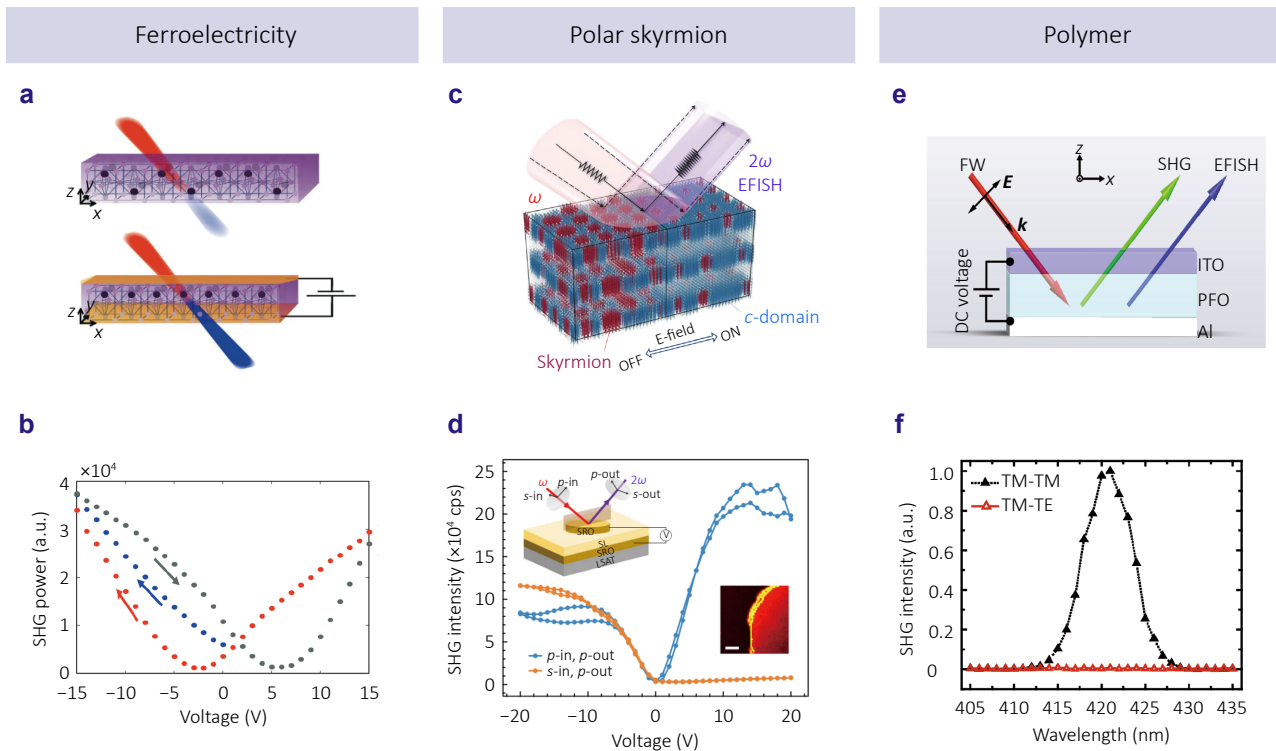


Fig. 4 | Bulk nonlinear material engineering for EFISH. (a) Schematic of the PZT thin film poled along the z-axis and the trajectories of the incident fundamental beam (ω , red) and the SH beam (2ω , blue). Black dots denote Ti/Zr ions, which define the film's polarization density. (b) Evolution of SHG power under a triangular DC bias: the bias starts from 0 V and follows the blue, gray, then red curves. The observed butterfly hysteresis in SHG confirms ferroelectric domain alignment in the PZT film. (c) Schematic of EFISH from Polar Skyrmion. (d) Measured SHG intensity versus applied voltage for *p*- (parallel) and *s*- (perpendicular) polarized fundamental light. Bias sequence: 0→20→-20→0 V. (e) Schematic of EFISH from the ITO/PFO/Al device. (f) Polarization dependence of SHG at 420 nm with TM polarization incident. The TM-TM (same as fundamental) polarized SHG signal is significantly stronger than the TM-TE (cross polarized) component. Figure reproduced with permission from: (a, b) ref.⁵¹, John Wiley and Sons; (c, d) ref.⁵², (e, f) ref.²⁰, Springer Nature.

heterostructures⁶⁸. Beyond layered engineering, transition metal dichalcogenides (TMDs), which exhibit C-exciton resonance in the visible/near-IR, leading to dramatic nonlinear enhancement⁶⁴. Therefore, the interplay between electrically biased centrosymmetric layers and excitonic resonance becomes a central lever for the EFISH studies in vdW materials⁶⁹.

A variety of multilayer TMDs exhibit inversion symmetry^{70–72}, a prime example of which is bilayer TMDs in hexagonal phase (2H) with AB stacking⁶⁴, which belong to the centrosymmetric D_{3d} point group. In EFISH research involving TMDs, the field-effect transistor (FET) geometry is commonly used, as it allows for efficient application of a vertical electric field to break inversion symmetry. For such D_{3d} symmetric bilayers, however, the required out-of-plane third-order susceptibility components for EFISH are forbidden. Consequently, no vertical EFISH emission is expected in this FET configuration. Microscopically, a uniform out-of-plane bias induces equal-magnitude but oppositely oriented in-plane dipoles in the two layers, thus their contributions cancel, preserving the overall inversion symmetry and suppressing EFISH. In practice, however, this electrostatic field is often layer-asymmetric⁷³, breaking the inver-

sion symmetry and inducing SHG due to its layer-related electronic dynamics. Strictly speaking, EFISH refers to a uniform, collective DC-field-induced asymmetric electrical polarization. Asymmetric polarization arising from spatially nonuniform layer-dependent electric fields does not constitute EFISH in the strict sense; therefore, this section covers electric-field-induced centrosymmetry-breaking mechanisms responsible for SHG in centrosymmetric vdW materials, using the original terminology from each paper rather than EFISH to avoid confusion.

For example, monolayer MoTe_2 exhibits intriguing phase-dependent symmetry characteristics, being centrosymmetric in the 1T' phase and non-centrosymmetric in the 1H phase. Wang et al. demonstrated that these distinct symmetry phases of MoTe_2 can be electrically controlled via electrostatic doping, which leads to a pronounced decrease in broadband SHG intensity associated with the transition from the non-centrosymmetric to centrosymmetric phase at a critical gate bias (approximately 3 V)⁷⁴, as illustrated in Fig. 5(a). This electrostatically driven phase modulation enables highly efficient SHG switching, characterized by an exceptional on/off ratio of 1000, a modulation strength of approximately 30,000% per volt and a broad operational

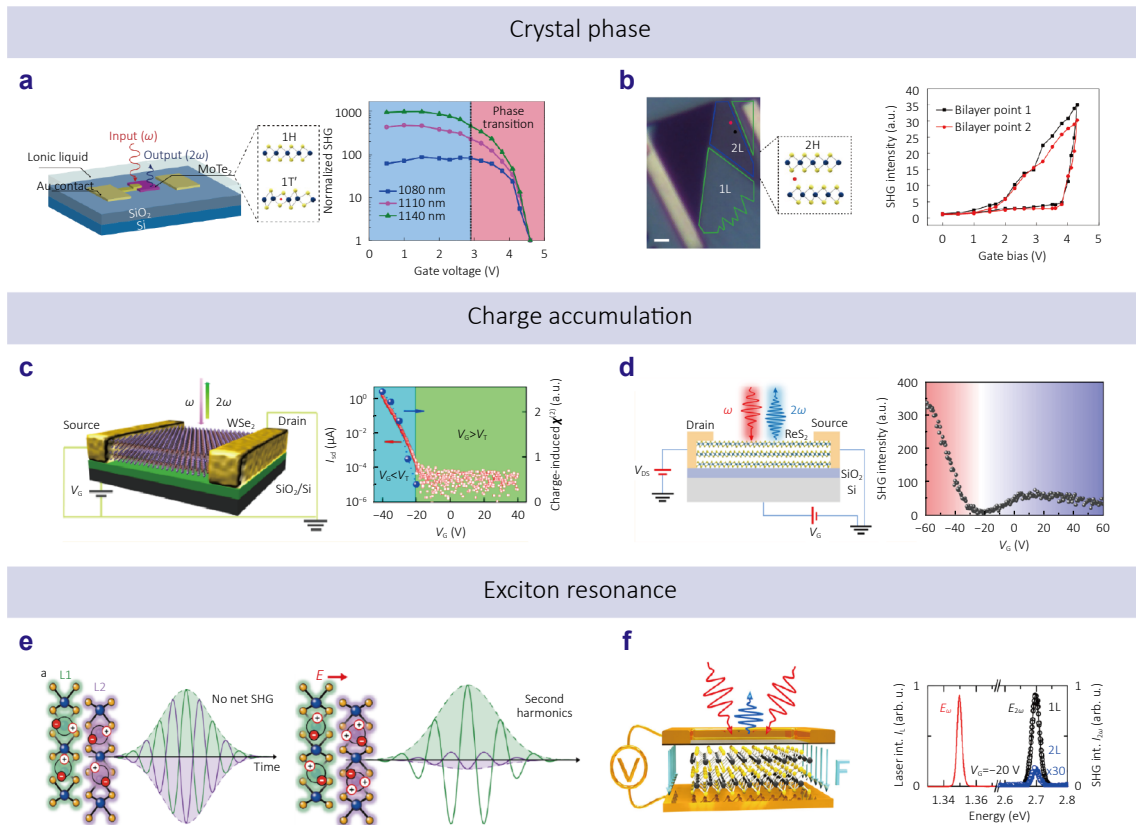


Fig. 5 | Electric-field-induced symmetry breaking in vdW materials. Crystal phase: (a) Schematic of an SHG modulator: ionic liquid provides electrostatic doping under gate bias V_G , driving a structural transition between the 1H and 1T' phases in monolayer MoTe₂. The inversion center (red dot) is present in the 1T' phase. (b) Optical micrograph of a mixed monolayer (1 L, green outline) and bilayer (2 L, blue outline) MoTe₂ flake contacted by electrodes (yellow rectangles). Gate-dependent SHG curves from two bilayer regions show opposite trends, with a sharp increase above 3.8 V, indicating inversion symmetry breaking. Charge accumulation: (c) schematic of the bilayer WSe₂ device configuration and source-drain current and voltage ($I_{sd} - V_G$) characteristics. Region I (blue $V_G < V_T$) drives hole accumulation (increasing I_{sd}) and region II (green $V_G > V_T$) where FET bias establishes a uniform out-of-plane electrostatic field. SHG intensities (blue dots) trace track on the $I_{sd} - V_G$ curve confirming the mechanism of charge accumulation induced SHG rather than EFISH. (d) Structure diagram of a trilayer ReS₂ FET. Excitation at ω (red arrow) generates SHG at 2ω (blue arrow). Gate-voltage dependence of SHG intensity in the trilayer device. Exciton resonance: (e) in 2H-stacked bilayer WSe₂, intralayer exciton states in each layer produce opposite SHG signals that cancel, yielding zero net SHG. Selective hole injection into one layer induces exciton-polaron states, while the other layer remains charge neutral, resulting in distinct resonances and enhanced SHG. Reproduced with permission⁷⁷. (f) Schematic of a bilayer MoS₂ microcapacitor with a semitransparent top gate for simultaneous optical access and gate bias V_G . Typical SHG spectra at $E_\omega=1.35$ eV for monolayer (black circles) and bilayer (blue circles, 30 x magnified) 2H-MoS₂ at $V_G=-20$ V, showing restored inversion symmetry in the bilayer. Figure reproduced with permission from: (a, b) ref.⁷⁴, Springer Nature; (c) ref.⁷⁵, (d) ref.⁷⁶, (e) ref.⁷⁷, (f) ref.⁷⁸, American Chemical Society.

spectral range of around 300 nm. Such a phase transition not only facilitates symmetry control in monolayers but also enables symmetry breaking in bilayer 2H-MoTe₂. Under FET bias, the upper layer undergoes a phase transition under electrostatic doping, whereas the lower layer retains its original phase, resulting in a SHG response distinct from that observed in monolayer MoTe₂, see Fig. 5(b).

Similarly, Huakang et al.⁷⁵ observed pronounced SHG in 2H-stacked bilayer WSe₂, induced by a back-gate voltage below the saturation point (approximately -20 V), as illustrated in Fig. 5(c). In this device, a negative gate voltage induces hole accumulation predominantly in the bottom WSe₂ layer, specifically forming localized $W_{5d_{x^2-y^2,xy}}$ orbitals, which prevents further electric field penetration

into the upper layer. This asymmetric charge distribution breaks the inversion symmetry, preventing cancellation of second-order bond hyperpolarizabilities and resulting in observable SHG. Under positive voltage bias, in contrast, only a depletion regime forms without significant charge accumulation. Consequently, symmetry breaking is minimal, and the resulting SHG signal remains negligible. This phenomenon, termed charge-induced SHG, arises explicitly from the layer-dependent spatial distribution of accumulated charges. A similar behavior was also observed in trilayers ReS₂⁷⁶, as illustrated in Fig. 5(d). However, in contrast to the explanation for hole accumulation for bilayer WSe₂, Wang et al. attributed the observed SHG to interlayer charge transfer, causing a vertical asymmetry in charge density

distribution as supported by first-principles calculations. The weak SHG signal under positive gate voltage is attributed to electron accumulation at the bottom sulfur layer, which leads to charge shielding. However, a decrease in SHG signal at gate voltages above 20 V remains unexplained, underscoring the need for further exploration of complex interlayer charge dynamics in vdW multilayers.

In addition to the above mentioned electric field-induced interlayer asymmetry in the electronic states, layer-dependent exciton resonances substantially amplify the SHG amplitude and its electrical modulation depth. For example, Soonyoung et al.⁷⁷ reported a 40-fold SHG enhancement in bilayer WeS_2 by leveraging strong exciton resonances and a layer-dependent exciton-polaron effect. By selectively localizing injected holes within one layer, exciton-polaron states are induced in the hole-rich layer, while normal exciton states persist in the charge-neutral layer. This distinct resonance condition effectively breaks interlayer inversion symmetry, thus promoting resonant SHG, see Fig. 5(e). Moreover, symmetry breaking induced by a perpendicular electrostatic field in bilayer MoS_2 was also studied by Klein J et al.⁶⁵. Layer-dependent exciton resonances arising from interlayer hybridization of sulfur orbitals result in the enhanced SHG intensity 60-fold, see Fig. 5(f)⁷⁸. This symmetry breaking can be visualized via calculations of the two-particle exciton wave functions over the Brillouin zone (BZ) as illustrated in Fig. 5 of the original work⁷⁸. At C resonance (upper panel MoS_2), the exciton wavefunction is weakly modified by the out-of-plane electric field. In contrast, in the lower panel, a slight detuning of the wave function leads to pronounced features near the Γ point. When a DC field is applied, the nonlinear polarizations become layer-asymmetric, which leads to a nonzero SH polarization. Recently, Okada et al.⁷⁹ reported that an exciton-resonance-enhanced EFISH-like phenomenon also exists in two-dimensional hybrid perovskites. The authors employed $(\text{BA})_2(\text{MA})_{n-1}\text{Pb}_n\text{I}_{3n+1}$ (with $n = 2$) as a host material and introduced a polar organic cation, *R*-MBACl, into the perovskite lattice. Under a vertical applied field, the polar *R*-MBA⁺ molecules reorient along the field direction, locally breaking centrosymmetry and enabling the EFISH process. Remarkably, when the SHG photon energy is tuned near the exciton resonance, the system exhibits a resonantly enhanced nonlinear response, with SHG intensity boosted by nearly two orders of magnitude.

Other two-dimensional materials, such as group IIIA-VIA compounds (e.g., GaSe, InSe, In_2Se_3 , Ga_2Se_3), group VIA monochalcogenides (MX, e.g., GeS, GeSe, SnS and SnSe) and hexagonal boron nitride (h-BN), have also shown great potential in nonlinear optics⁸⁰. In particular, GaSe and InSe only exist in three distinct crystalline structure types^{81–84}. Although EFISH-like effect is expected in these materials, it has not been observed yet, which makes them promising candidates for future EFISH studies. Furthermore, MX monochalcogenides have been predicted to be two-dimen-

sional ferroelectric materials^{85,86}. Inspired by the EFISH effect in bulk ferroelectric materials^{51,62}, group VIA monochalcogenides are expected to exhibit outstanding EFISH response.

2.1.3 Polymers

Organic conjugated polymers, particularly π -conjugated systems, facilitate significant electron delocalization and thus exhibit large hyperpolarizabilities^{87–92}. However, fundamental studies of EFISH in polymer materials remain quite limited. To the best of our knowledge, only Shumei et al.²⁰ reported that a 25-fold EFISH enhancement can be achieved due to band-edge effects in an organic p-type π -conjugated polymer (PFO, poly(9,9-di-*n*-dodecylfluorenyl-2,7-diyl)). Their device consists of a 100 nm thick film of organic conjugated polymer PFO sandwiched between aluminum and ITO, as illustrated in Fig. 4(e). Under an incident fundamental wave with a 45-degree transverse magnetic (TM) polarization, the reflection spectrum exhibits strong absorption below 400 nm, corresponding to a bandgap energy of 2.95 eV. When the fundamental photon energy is half of the peak absorption energy (at 840 nm), a 25-fold enhancement in SHG intensity (under 6 V bias) and modulation ratio of up to 422% V^{-1} were achieved, as illustrated in Fig. 4(f). This resonance-like behavior, referred to as the band-edge effect, arises when the SH photon energy approaches the bandgap of the polymer. However, the microscopic mechanism underlying this effect remains unclear.

To conclude this section, research on EFISH materials emphasizes unusual electronic properties, such as ferroelectricity, electronic skyrmions, exciton resonances, and band-edge effects. These centrosymmetric systems exhibit intrinsically weak SHG and high sensitivity to externally applied electrostatic fields, enabling large EFISH modulation depths. However, most prior studies focused on thin films with externally biased electrodes, with an emphasis on the intrinsic material properties. Beyond the choice of materials, device-level structural engineering (tailoring the DC-field distribution, optical confinement, phase matching, and transverse modal overlap) offers a clear route to further enhance performance, as discussed in the following section.

2.2 Engineering of E_{DC}

The electrostatic field arises from a spatially non-uniform charge distribution with the description of the Poisson equation⁹³. Common charged species include free electrons and holes, lattice ions, ionized dopants, or defects⁹⁴. Engineering E_{DC} for EFISH therefore relies on the manipulation of these charged species.

2.2.1 External electrodes

The most established method to introduce an electrostatic field is to manipulate the spatial distribution of free electrons in conductors. When conductors are connected to an

external bias, abundant delocalized electrons rapidly redistribute and accumulate at the surface, rendering the conductor equipotential. The resulting surface charge at the conductor interface enforces the electrostatic boundary conditions and establishes potential difference in the intervening medium. In the most straightforward configuration, an insulator is placed between metallic electrodes of different voltages. The electrostatic field inside the insulator is well approximated as homogeneous with magnitude defined primarily by the applied voltage $E_{DC} = \Delta V/d$ (where ΔV is the applied voltage and d is the distance between electrodes). Consequently, simulations of the DC field agree closely with measured EFISH maps, and the SHG intensity exhibits the expected quadratic dependence on the applied voltage ($I_{2\omega} \propto (\chi^{(3)} : E_{DC} : E_{\omega} \otimes E_{\omega})^2 \propto \Delta V^2 I_{\omega}^2$)^{17,95}.

However, when the intervening medium is a semiconductor (e.g., in metal-oxide-semiconductor (MOS)⁹⁵ or metal-semiconductor-metal (MSM)⁹⁶ structures), carrier dynamics in the semiconductor layer under bias cannot be neglected. At thermal equilibrium, the band alignment at the metal-semiconductor interface results in the formation of a Schottky barrier or Ohmic contact. In EFISH, it is the band bending with symmetric electron population in momentum space that breaks the inversion symmetry (Fig. 3(c)), thus EFISH signals primarily arise within the carrier depletion regions induced by the Schottky barriers⁹⁷. External voltage modulates both the width and magnitude of the depletion-region field, leading to a linear relationship between the electrostatic field and applied bias. Experimentally, this field modulation manifests as a parabolic dependence of the EFISH signal intensity on the applied voltage within the depletion regime^{98,99}.

Beyond the classical Schottky mechanism, in certain materials, high-field domain form, capable of sustaining strong and uniform internal electrostatic fields. For example, in GaAs¹⁰⁰, high-field domains emerge due to electron scattering into satellite valleys of the conduction band, thus reducing electron mobility at elevated fields. Similarly, in CdS^{101,102}, holes trapped at the defect sites become ionized under strong fields and subsequently recombine with conduction electrons, decreasing the free carrier concentration. This field-quenching mechanism results in the establishment of distinct high- and low-field domains. Recently, high-field domains have been experimentally observed in CdS nanostructures⁹⁶, as depicted in Fig. 6(a). As the reverse bias voltage increases, the Schottky barrier broadens, triggering the formation of high-field domains and consequently yielding nonlinear SHG intensity voltage characteristics. Three distinct operational regimes are discernible in Fig. 6(b): (i) weak EFISH dominated by the Schottky field for $V_{DS} < V_T$; (ii) formation and growth of a high-field domain for $V_T < V_{DS} < V_C$; and (iii) saturation of field amplitude for $V_{DS} > V_C$. This high-field domain forms due to electron excitation from the valence band to deep accep-

tor states, which upon ionization become negatively charged, stabilizing the domain. Increasing the voltage further expands the spatial extent of this domain until saturation occurs.

Another effective way to establish a nearly uniform internal electric field is the p-i-n junction. In this architecture, carrier diffusion across the p-i and i-n interfaces creates a wide depletion region in the intrinsic layer; the uncompensated ionized dopants in that region then sustain a built-in electric field throughout the i-region. Timurdogan et al.¹⁰³ design an EFISH-enabled quasi-phase matching (QPM) grating in silicon p-i-n waveguides as illustrated in Fig. 6(c). By engineering periodic p-i-n junctions, quasi-phase matching between fundamental and second-harmonic was achieved, yielding a peak conversion efficiency of 13 W^{-1} and an effective second-order susceptibility $\chi_{\text{eff}}^{(2)} = 41 \text{ pm/V}$ at a wavelength of $2.29 \mu\text{m}$, see Fig. 6(d).

In addition, Jasinskas et al.¹⁰⁴ report an EFISH design using inter-digitated electrode structures. They employed direct laser ablation to pattern comb-shaped electrodes in a thin chromium film deposited on a transparent glass substrate. An organic polymer layer was then coated atop these electrodes as the nonlinear optics material. By applying alternating DC biases across adjacent electrode fingers, a spatially periodic nonlinear-susceptibility grating of alternating $+\chi_{\text{eff}}^{(2)}$ and $-\chi_{\text{eff}}^{(2)}$ regions is established, enabling second-harmonic diffraction, see Fig. 6(e, f).

Apart from external DC voltage biasing, internal DC fields can also be induced by the Maxwell-Wagner (MW) effect under high-frequency AC voltages¹⁰⁵. The MW effect originates from charge accumulation at interfaces between materials with mismatched dielectric constants and conductivities. Although MW-induced EFISH (MW-EFISH) is generally considered negligible due to weak and localized field formation at sharp interfaces, graded interfaces formed via diffusion can enable more extended internal DC fields. Recently, Scherbak et al.¹⁰⁶ demonstrated MW-EFISH in ion-exchanged soda-lime glass, where accumulated interfacial charge generated internal fields as high as 10^8 V/m , boosting SHG by over two orders of magnitude.

2.2.2 Photo-induced field

In addition to externally applied biases, an electrostatic field can be generated via optically induced spatial carrier redistribution, giving rise to all-optical EFISH effect. This effect arises when photoexcitation carriers become spatially separated and accumulate as a net space charge, which is governed by three critical factors: (i) density of states (DOS): high DOS of electron donors and acceptors enhances free electron excitation and injection rates, respectively; (ii) asymmetric separation of carriers: the directionality and efficiency of electron-hole separation set the sign and magnitude of the built-in electrostatic field; and (iii) carrier lifetime: the lifetime of trapped electrons directly determines

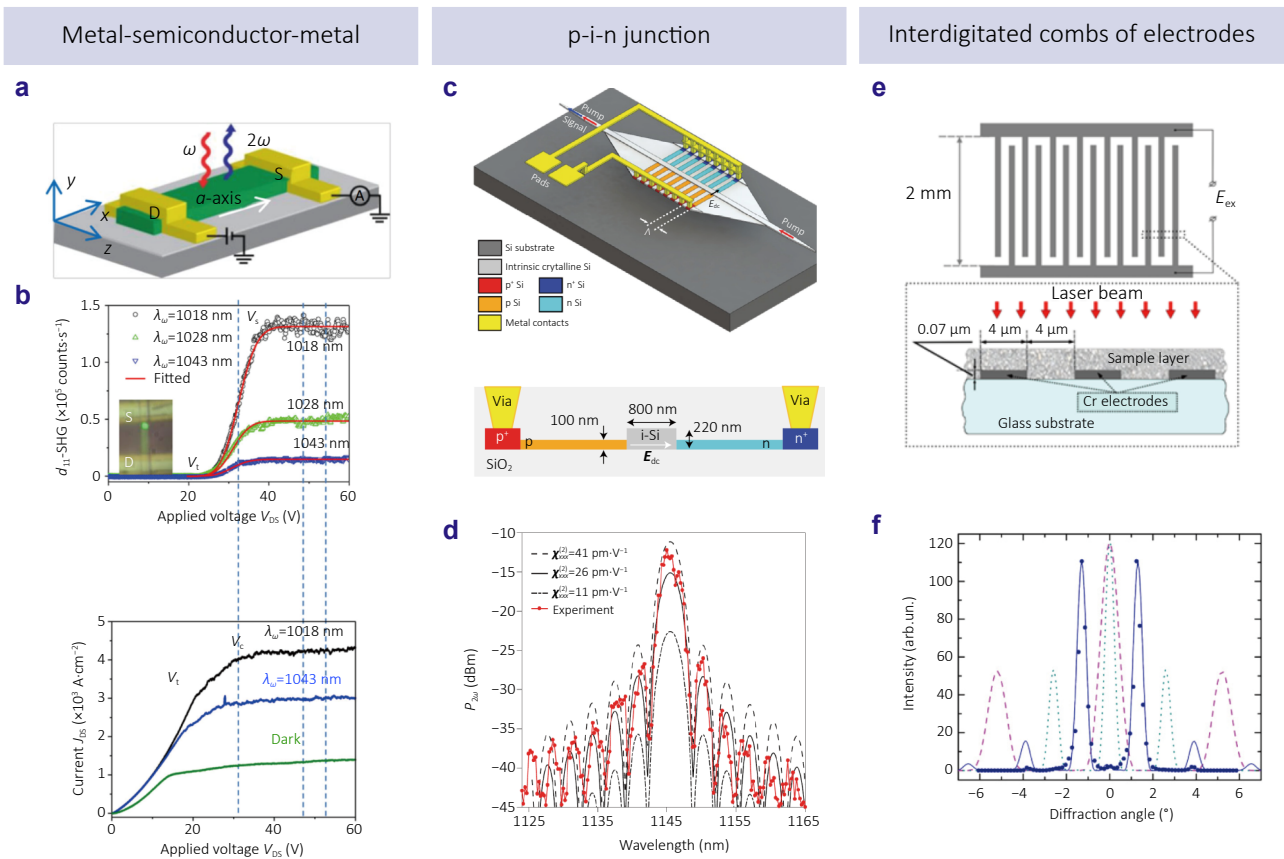


Fig. 6 | Electrostatic field engineering in EFISH. Metal-semiconductor-metal: (a) schematic of the CdS nanobelt device with source (S) and drain (D) electrodes. (b) Position dependence of the d_{11} SHG signal. Inset: optical micrograph showing the FW incident near the grounded source electrode (S, 0 V) while the drain electrode (D) is biased. Under positive V_{DS} , current flows along the x-axis from D to S, reverse-biasing the S contact. d_{11} -SHG signal scanned over the entire nanobelt from the source to drain electrodes at $V_{DS}=30$ V. p-i-n junction: (c) schematic of EFISH device with silicon ridge waveguide and quasi-phase-matched spatially periodic patterning of the p-i-n junction. (d) On-chip SHG intensity curves for estimated second-order susceptibilities. Interdigitated combs of electrodes: (e) schematic of interdigitated electrode combs: top-view and side-view. E_{ex} denotes the applied external electric field. (f) Angular dependence of the EFISH intensity: experimental data (points) and calculation (solid blue line). Dashed magenta and dotted green lines show the calculated Fraunhofer diffraction patterns for the fundamental and second-harmonic signals, respectively. Figure reproduced with permission from: (a, b) ref.⁹⁶, (c, d) ref.¹⁰³, Springer Nature; (e, f) ref.¹⁰⁴, Optical Society of America.

the lifetime of the electrostatic field. For example, in continuous media under a uniform illumination, independent absorption events produce a spatially uniform carrier distribution, thus no net space charge forms. A space-charge regime arises only when carrier distribution is asymmetrical (e.g., when gradient electrochemical potential between donor and acceptor^{107,108} or the interference among distinct multiple-photon absorption pathway^{109–111} bias carrier motion). Additionally, the space-charge regime decays over time because of the carrier recombination. Its lifetime varies considerably, ranging from femtoseconds in ultrafast processes to seconds or even longer in defect-stabilized systems, largely dependent on the depth of the acceptor states. Consequently, the induced field typically increases during the first few hundred seconds of illumination, gradually approaching saturation, and decays after the illumination is turned off.

A standard route to establish an electrochemical-potential gradient is to form a junction between different Fermi levels. Upon contact, band alignment induces a built-in electrostatic field within the depletion region near the interface. Under thermal equilibrium, this electrostatic field is time-independent and spatially localized at the interface. Thus, EFISH coexists with surface SHG, and they should be somehow distinguished. Under photoexcitation, however, photon absorption generates free carriers that modify the depletion region¹²¹. This modification is synchronized with the carrier dynamics and the saturated field amplitude scales linearly with the pump intensity. Consequently, EFISH intensity becomes time-dependent and scales quadratically with the pump intensity. This different scaling allows discerning EFISH from surface contribution to SHG experimentally.

An extensively studied platform for charge-transfer-induced EFISH is the Si/SiO₂ junction, where Si serves as the

electron donor and SiO₂ as the acceptor^{112–119}. The Si band gap of approximately 1.1 eV and the Si/SiO₂ conduction band offset of ~3.2 eV require multiphoton energy to exceed ~4.3 eV. When the fundamental photon energy exceeds 1.36 eV, electrons in silicon can be promoted into defect states at the SiO₂/Si interface via three-photon absorption or direct absorption of the third-harmonic photon¹²⁰. At higher photon energies and excitation intensities, increased free-carrier generation and associated space-charge screening lead to a deviation from quadratic scaling in the SHG intensity. Once the field saturates, the SHG intensity scales quadratically with pump power, reflecting an

intensity-independent steady-state field^{108,121}.

Similar behavior has been demonstrated in metal-semiconductor heterojunctions. In particular, plasmonic metal nanostructures leverage localized surface plasmon resonance (LSPR) to enhance near-field intensities and facilitate ultrafast charge transfer¹²² attracting researchers' attention. For example, Yali et al.¹²³ demonstrated a hybrid EFISH nanoantenna comprising a gold nanoparticle atop a silicon nanocone as illustrated in Fig. 7(a). Under 1047 nm (1.18 eV) illumination, electrons transfer from silicon to gold breaking through the Schottky barrier, generating a static field of ~10⁸ V/m at the Au/Si contact. The sub-quadratic

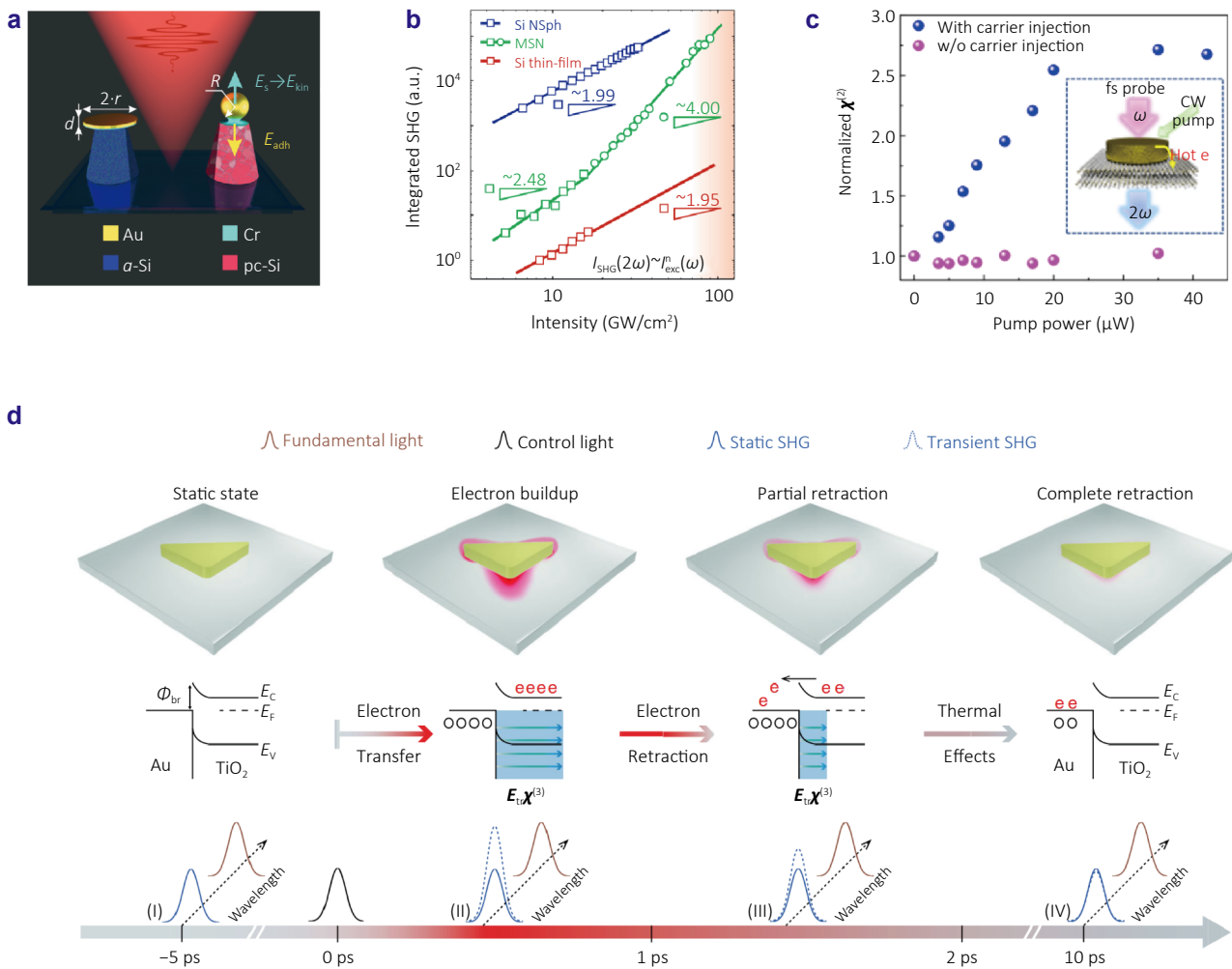


Fig. 7 | Optical induced EFISH in heterogeneous structures. (a) Schematic of the hybrid MSNs. (b) Evolution of the instantaneous slope of the SHG intensity versus excitation power in a log-log plot. Both the silicon nanostructured single particle and the thin film exhibit a quadratic dependence of SHG intensity on pump power, characteristic of conventional second-order nonlinear processes. In contrast, the optically induced EFISH process demonstrates a clear deviation from the quadratic behavior, indicating a non-quadratic power dependence. (c) Illustration of the plasmon induced hot electrons form Au nanobar transfer to bilayer WSe₂, which establish a nonstatic separation electric field at the interface perturbation the centrosymmetry and produce SHG. (d) Mechanism of inversion-symmetry breaking by hot-electron transfer: (top) plasmon excitation produces and injects hot electrons into the dielectric; (middle charge separation across the Schottky junction creates a transient field E_{tr} , converting the host's $\chi^{(3)}$ response into an effective $\chi_{eff}^{(2)} \propto \chi^{(3)} : E_{tr}$; (bottom) the combined effect of asymmetric electron injection and E_{tr} breaks the crystal symmetry, enabling ultrafast all-optical control of second-order nonlinear processes such as SHG. Figure reproduced with permission from: (a, b) ref.¹²³, Springer Nature; (c) ref.¹³³, American Chemical Society; (d) ref.¹³⁴, American Physical Society.

scaling of SHG intensity with pump power in a log-log plot confirms the EFISH mechanism, see Fig. 7(b), while the tens-of-seconds saturation time reflects carrier trapping and detrapping at interface defects. Moreover, LSPR decay generates hot electrons with energies exceeding the Schottky barrier, which are injected into conduction bands of the adjacent semiconductor on picosecond timescales, transiently breaking inversion symmetry and driving ultrafast EFISH^{124–129}. Coulomb forces then return carriers into the metal over femto- to picosecond timescales^{130–132}. Wen et al.¹³³ confirmed this mechanism by observing enhanced SHG from gold nanobars on bilayer WSe₂, as illustrated in Fig. 7(c), which was suppressed by inserting an hBN interlayer to block hot-electron transfer. Similarly, Taghinejad et al.¹³⁴ reported transient SHG in amorphous TiO₂ induced by asymmetric hot-carrier injection from triangular gold nanostructures, yielding SHG transients that mirror hot-electron relaxation dynamics as illustrated in Fig. 7(d).

Another way to introduce directionality to free carriers is through interference between multiple photon absorption pathways, where the carrier flux is controlled by the relative phase between the FH and SH fields^{135–138}. The total ionization rate from multiphoton absorption is described by¹³⁹:

$$\begin{aligned} \dot{\rho}_{\pm} = & R (|E_{2\omega}|^4 + \eta_3^2 |E_{2\omega}|^2 |E_{\omega}|^4 + \eta_4^2 |E_{\omega}|^8) \\ & + \eta_4 |E_{2\omega}|^2 |E_{\omega}|^4 \exp [2i (\phi_{2\omega} - 2\phi_{\omega})] \\ & \pm \{ -i\eta_3 |E_{2\omega}| |E_{\omega}|^2 (\eta_4 |E_{\omega}|^4 - |E_{2\omega}|^2) \\ & \cdot \exp [i (\phi_{2\omega} - 2\phi_{\omega})] \} + c.c., \end{aligned} \quad (6)$$

where E_{ω} and $E_{2\omega}$ are the local electric fields of the fundamental and second harmonic waves, respectively, ϕ_{ω} and $\phi_{2\omega}$ are their phases, and η_i are the multiphoton absorption coefficients. The first term corresponds to independent multiphoton absorption processes, involving four FH photons, two FH photons combined with one SH photon, and two SH photons. The second term describes the interaction between the four-FH and the combined two-FH-one-SH photon absorption processes. The final term represents the interaction among all three multiphoton absorption processes inducing asymmetric photoelectron emission. The subsequent capture of these asymmetrically emitted electrons by deep trap states at the boundaries of the illuminated region results in a substantial built-in electrostatic field. This field grows until the photocurrent ($j_{ph} \sim \dot{\rho}_+ - \dot{\rho}_-$ due to anisotropic electron emission) is balanced with the conduction current.

Specifically, the phase in the third term makes the field periodic, forming an effective $\chi^{(2)}$ grating via EFISH^{140,141}. This grating provides an external momentum to satisfy the phase-matching condition for SHG spontaneously^{142,143}:

$$\mathbf{k}_{DC} = \frac{\partial}{\partial r} (\phi_{2\omega} - 2\phi_{\omega}) = \mathbf{k}_{2\omega} - 2\mathbf{k}_{\omega}, \quad (7)$$

where \mathbf{k}_{DC} is the reciprocal-lattice vector of this second-order nonlinear susceptibility grating, and $\mathbf{k}_{2\omega}$ and \mathbf{k}_{ω} are the

wave vectors of the SH wave and FH, respectively. This phenomenon is known as coherent photogalvanic effect (CPE).

For observable SHG via CPE, two conditions must be fulfilled: (1) initial seed SHG, potentially arising from interface states or intrinsic nonzero higher-order electric multipole (e.g., quadrupole) polarization distributions, and (2) accumulation time sufficient for the space-charge field to build.

This phenomenon was first observed in glass optical fibers¹⁰⁹ and subsequently demonstrated in Si¹¹¹, Si₃N₄¹³⁵ and GaAs¹⁴⁴. Direct visualization of the induced gratings was accomplished by chemically etching germanosilicate fibers using hydrofluoric acid, as the etching rate is sensitive to the intensity of the internal electric field¹⁴⁵. Recently, silicon nitride (Si₃N₄)¹³⁵, characterized by ultralow optical losses and compatibility with integrated photonic and quantum technologies, has emerged as a promising platform for CPE studies. In Si₃N₄, nitrogen vacancies saturated by hydrogen atoms form Si–H and covalent Si–Si bonds, introducing defect states approximately 1.4 eV away from both the conduction and valence band edges within its band gap of approximately 4.6 eV. A multiphoton absorption mechanism involving two FH photons and one SH photon (collectively corresponding to 3.2 eV at a wavelength of 1500 nm) supports the hypothesis that these Si–Si defect states facilitate asymmetric carrier injection.

The first experimental demonstration and theoretical analysis of CPE in Si₃N₄ waveguides were presented by Adrien et al.¹³⁵ as illustrated in Fig. 8(a). They optically induced QPM using a continuous wave laser pump, achieving an effective nonlinear susceptibility $\chi^{(2)}$ of 0.3 pm/V and a maximum SHG conversion efficiency of 0.05% W⁻¹, consistent with coherent photogalvanic theory. Further, Edgars et al.¹⁴¹ addressed that variations in waveguide dimensions significantly affects the properties of the $\chi^{(2)}$ grating formed. Due to the coherent contributions of multiple SH modes, the resulting grating reflects a weighted superposition, with κ_{12} determining their cumulative impact on the effective refractive index $n_{eff}^{2\omega}$, which changes the grating period, see Fig. 8(b).

The above-mentioned early studies used continuous-wave (CW) illumination to inscribe the space-charge grating, whereas the advent of femtosecond pulses now provides a far more powerful tool for charge generation. However, for efficient inscription with ultrashort pulses, phase matching (spatial overlap) is not sufficient as group-velocity matching (temporal overlap) must be considered. Hickstein et al.¹³⁶ demonstrated that matching of group velocities minimizes the temporal walkoff between FH and SH waves, enabling continuous and efficient interference of the material with two fields simultaneously, thus enhancing spatial charge separation as illustrated in Fig. 8(c). The conversion efficiency of 0.005% W⁻¹ with an effective $\chi^{(2)}$ of 0.5 pm/V at

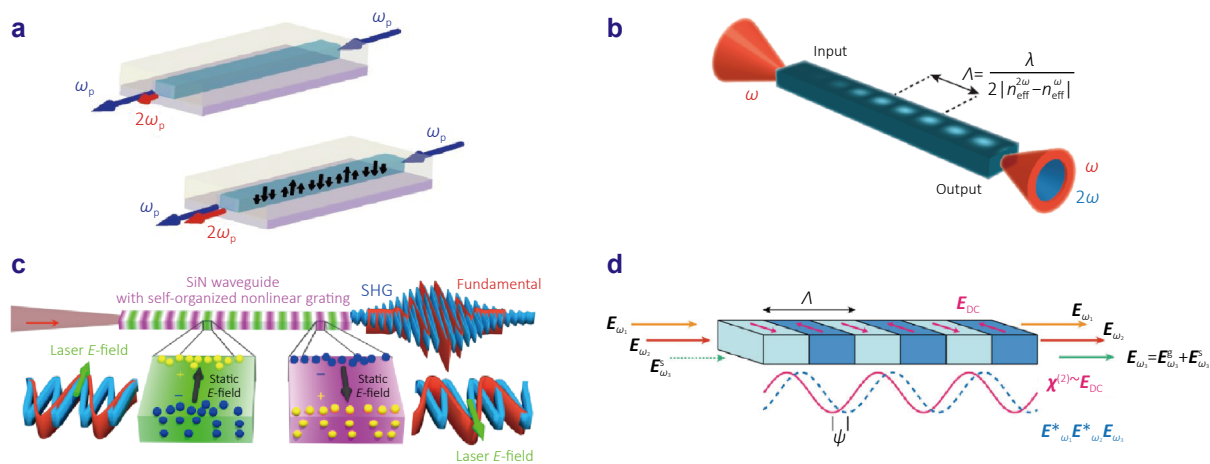


Fig. 8 | Optically inscribed $\chi^{(2)}$ gratings in a SiN waveguide. (a) Illustration of $\chi^{(2)}$ grating inscription: upon irradiation by a pump at frequency ω_p , a spatially periodic DC field develops with period which is the coherence length between the pump and second-harmonic modes. (b) Self-grating formation rules: the inscribed grating follows the spatial modulation of the nonlinear polarization, producing a self-organized quasi-phase-matched structure. (c) Charge-separation driven by pulse: interference between the fundamental pulse and second-harmonic pulse drives positive charges to one side of the waveguide and negative charges to the opposite side, establishing an electrostatic field that induces an effective $\chi_{\text{eff}}^{(2)}$ grating. (d) QPM grating for SFG schematic: an optically inscribed grating with period Λ can exhibit a relative phase shift ψ between the $\chi_{\text{eff}}^{(2)}$ modulation and the nonlinear polarization pattern of the interacting fields. Figure reproduced with permission from: (a) ref.¹³⁵, Springer Nature; (b) ref.¹⁴¹, ref.American Chemical Society; (c) ref.¹³⁶, Springer Nature; (d) ref.¹⁴³, John Wiley and Sons.

1560 nm was observed experimentally. Furthermore, Edgars et al.¹⁴⁶ demonstrated that maximizing the SHG conversion efficiency and bandwidth requires minimizing the wavelength dependence of the propagation constant mismatch ($\Delta\beta$). Mathematically, the condition $\partial\Delta\beta/\partial\lambda \approx 0$, equivalent to the group velocity matching condition, achieves this optimization. However, even with group velocity matching, this conversion efficiency remains low. The key issue is the limitation of the grating length. In order to understand the mechanism behind this limitation. Ozan et al.¹⁴³ further extended theoretical frameworks, including the initial phase difference (ψ) between the seed SH polarization (SH_S) and the generated SH polarization (SH_G) via CPE. Within slowly varying envelope and undepleted pump approximations, Maxwell equations yield the following expression governing SH generation dynamics¹⁴³:

$$\frac{\partial^2 \bar{\mathbf{E}}}{\partial t \partial z} - \frac{3\omega\chi^{(3)}}{2n_{2\omega}c\epsilon} \beta |\mathbf{E}_\omega|^4 \exp\left[i\left(\frac{\pi}{2} - \psi\right)\right] g^4(z) \bar{\mathbf{E}} = 0, \quad (8)$$

where $\bar{\mathbf{E}} = \mathbf{E}_{2\omega} e^{t/\tau} e^{az/2}$, $\tau = \epsilon/\sigma$ denotes the electrical relaxation time, where ϵ is the dielectric constant and σ the photoconductivity, α represents the SH propagation loss coefficient. The parameter β denotes the photogalvanic coefficient characterizing the efficiency of coherent current generation via multiphoton absorption interference, and $g(z)$ accounts for the walk-off between the pump and SH wave. At early propagation stages, the grating is predominantly written by the SH_S and constructively supports SH_G . However, as the SH_G grows and coherently interferes with the seed, the grating phase becomes self-consistently modified, leading to partial cancellation of the space-charge

modulation. Together with the concurrent increase in photoconductivity, this feedback drives the grating into a dynamical steady state, thereby limiting its effective spatial extent. This comprehensive model not only explains the phenomenon why the grating length is always limited, but also predicts the sum-frequency generation (SFG) QPM gratings, see Fig. 8(d).

To overcome limited grating lengths and enhance the effective interaction length and conversion efficiency, combining the CPE with resonant optical modes with a high Q factor appears promising. Specifically, whispering gallery mode (WGM) microring, characterized by ultrahigh Q factors and minimal mode volumes V , offer an excellent choice^{147–155}. The structural analogy between microring and bent waveguides shifts the mode-matching requirement to angular momentum matching. Wu XY et al.¹³⁷ first demonstrated that an initially seeded SH field and the FH generate a DC electric field via the photoelectric effect in a SiN microring resonator. Achieving perfect phase matching between SH and FH eigenmodes resulted in a uniform DC field up to 1×10^7 V/m as illustrated in Fig. 9(a), realizing an SHG conversion efficiency of $2500\% \text{ W}^{-1}$ (absolute efficiency of 22%). Edgars et al.¹³⁸ further showed that DC fields automatically compensate for the angular momentum mismatch if the SH and FH eigenmodes do not have perfect phase matching as illustrated in Fig. 9(b). Furthermore, Jianqi et al.¹⁵⁶ observed analogous CPE-induced SFG processes in Si_3N_4 microcavities, effectively yielding third-harmonic generation via FH-SH sum-frequency interactions. Both SHG and SFG gratings were experimentally

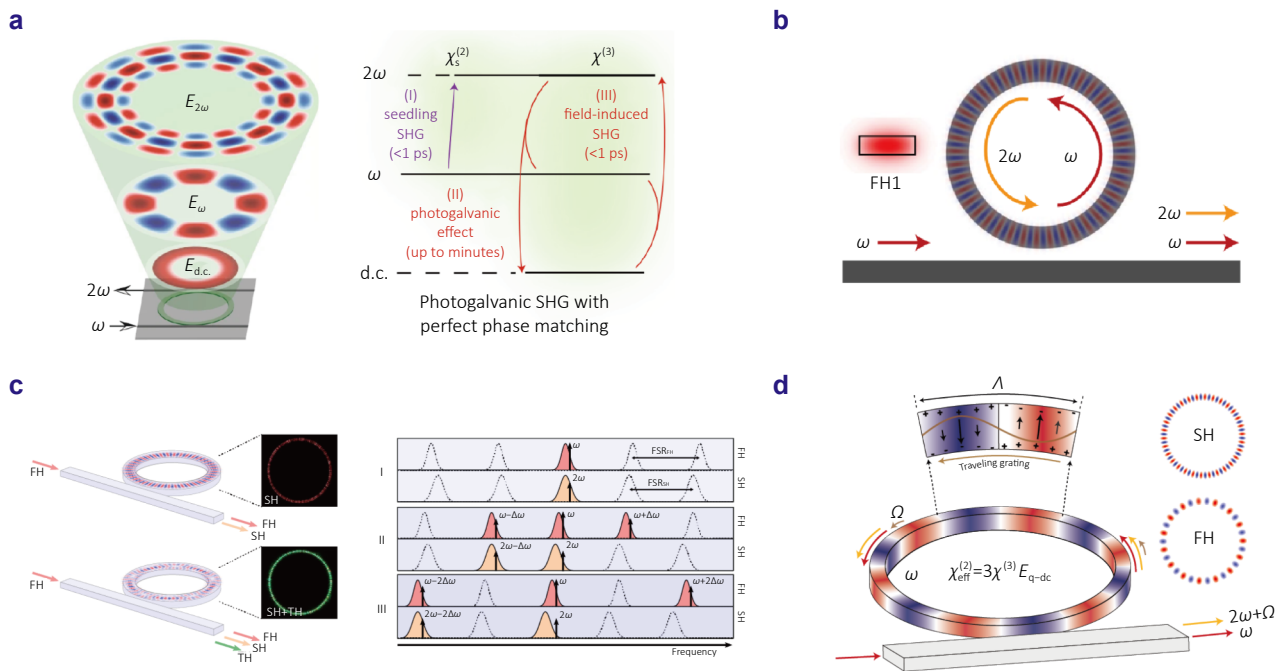


Fig. 9 | Optically inscribed $\chi^{(2)}$ gratings in a SiN microring (a) SHG via CPE with perfect phase matching. Illustration of the modes involved in perfect phase matching. Within the microring, the mode profiles of three interacting modes at ω , 2ω and d.c. frequencies are shown from top to bottom. Perfect phase matching induced uniform azimuthal distribution electrostatic field via CPE in a Si_3N_4 microring. Three-step photogalvanic SHG build-up: (I) a weak intrinsic $\chi_s^{(2)}$ seeds an initial SH field at 2ω ; (II) interference of the ω and 2ω fields generates a quasi-static DC field via the CPE; (III) the DC field and pump produce additional SH via CPE, together amplifying the SHG signal. (b) CPE compensating momentum mismatching spontaneously. Coupling of the fundamental mode (FH1, ω) with SH modes inscribes $\chi^{(2)}$ grating. The azimuthal distribution dc electrostatic field compensate the mismatch between FW and SH modes spontaneously. (c) The SFG process via CPE compensating momentum mismatching in microring. Momentum conservation of SHG, SFG and cascade THG = SHG+SFG: quasi-phase matching of SH, SF, and effective THG by the inscribed $\chi^{(2)}$ grating are demonstrated. (d) Spatiotemporal CPE: under doubly resonant conditions, the pump at ω inscribes a traveling $\chi^{(2)}$ grating oscillating at Ω , generating SH at $2\omega + \Omega$; spatial and temporal modulation of $\chi^{(2)}$ governs momentum and energy conservation. Figure reproduced with permission from: (a) ref.¹³⁷, (b) ref.¹³⁸, (d) ref.¹⁵⁷, Springer Nature; (c) ¹⁵⁶, AAAS.

demonstrated as illustrated in Fig. 9(c). Recently, it has been found that the CPE entails a temporal oscillation to reach a stable dynamical equilibrium¹⁵⁷, which makes the SH frequency detune with a kHz scale shift as illustrated in Fig. 8(d).

In conclusion, this section has summarized two principal routes to establish the static field in the centrosymmetric material: (i) external electrodes applied and (ii) optically induced field. In the latter, the electrostatic field and optical field are correlated. This correlation makes the EFISH $\chi_{eff}^{(2)}$ amplitude, spatial distribution, and temporal evolution dependent on the FH, leading to non-quadratic scaling of SH-FH intensity¹²³, $\chi_{eff}^{(2)}$ grating¹³⁶ and temporal evolution of SH intensity¹³⁴. Notably, CPE-induced $\chi_{eff}^{(2)}$ grating offers strong promise for nonlinear microscale, on-chip devices with high conversion efficiency. However, a key limitation is that the operating wavelength is constrained by the material band gap, and demonstrations to date remain restricted to a relatively small materials set (e.g., SiO_2 ¹⁰⁹, Si_3N_4 ¹³⁵). Expanding CPE-capable platforms with low-loss media would open access to wider wavelength ranges.

2.3 E_{ω} engineering

The fundamental optical field E_{ω} is the result of the excitation of the photonic eigenmode near ω . Accordingly, three ingredients govern E_{ω} : (i) mode profile at the pump frequency; (ii) efficiency of mode excitation, and (iii) the resulting field enhancement inside the resonator. Optical eigenmodes are solutions of Maxwell equations with spatial refractive distribution $n(r)$ (analogous to eigenstates of the Schrödinger equation in a potential well, $n(r)$ act as the artificial optical potential of photons). In highly symmetric structures, photonic modes carry quantum numbers and the nonlinear processes require the conservation of these quantum numbers as discussed in Section 2. Consequently, the symmetry of the structure, together with the orientation of the nonlinear susceptibility tensor, determines the symmetry properties of the eigenmodes and defines the selection rules for both linear and nonlinear modes excitation.

A canonical example is Mie theory, where the situation is relatively straightforward, as each eigenmode corresponds to a single multipolar contribution (e.g., dipole, quadrupole, octupole)¹⁵⁸. In contrast, for resonators with reduced symmetry, these rules become more complex, since modes

can couple via multiple multipolar channels. Nevertheless, symmetry analysis enables one to predict the multipolar composition of each mode, which is essential for understanding high-Q quasi-BIC resonance, anapole, and exceptional point (EP)^{28,159–161}.

Metasurfaces, consisting of subwavelength "meta-atoms" arranged in a 2D lattice, have emerged as a versatile platform for controlling photonic modes. A key advantage of metasurfaces is the design freedom in both unit cell and lattice symmetries, which allows for precise manipulation of light. For example, breaking the lattice symmetry alone can result in the emergence of chiral modes¹⁶². Meanwhile, in-plane unit cell symmetry plays a critical role in both phase and amplitude of the scattered wave (e.g., C_2 symmetry controlling Q factor of quasi-BICs^{163–166}, rotation-controlled phase profiles underpinning the generalized Snell law¹⁶⁷). In particular, the resonant enhancement of the fundamental electric field can boost SHG efficiency by several orders of magnitude, achieving enhancements of up to a thousand-fold^{168–176}.

The field enhancement capability of one mode is defined by the Q/V ratio, where Q is the total Q factor of the mode and V is the adequate mode volume. In plasmonic structures, the field enhancement is determined by the small mode volume, while for most dielectric structures, the mode volume is about λ^3 and the field enhancement is defined by the Q . In the scatter systems, the Q is defined as, $Q = \omega_0/2\gamma_0$, where ω_0 and γ_0 are the real and imaginary parts of the complex eigenfrequency, representing the resonance frequency and the loss (decay rate) of the leaky mode, respectively. And the loss γ_0 accounts for both radiative loss $\gamma_{0,r}$ and non-radiative loss $\gamma_{0,nr}$ ($\gamma_0 = \gamma_{0,r} + \gamma_{0,nr}$). Various types of systems can provide high Q resonance, including photonic crystal cavities, BIC-supporting metasurfaces¹⁷⁷, plasmonic structures^{168–171}, and Mie-resonant nanostructures^{171–176}.

For EFISH on a resonant metasurface, the radiated SH power is governed by three ingredients: in-coupling of the incident wave to the FH mode, nonlinear coupling between FH and SH mode and out-coupling of the SH eigenmode to the far field:

$$\begin{aligned}
 P_{2\omega} \propto & \left[\underbrace{P_\omega \times \kappa_{\text{FH}} L_{\text{FH}}(\omega)}_{\text{FH in-coupling}} Q_{\text{FH}} \right]^2 \\
 & \times \underbrace{\left\{ \int_V \mathbf{E}_{\text{SH}} \cdot [\chi^{(3)} : \mathbf{E}_{\text{DC}} : (\mathbf{E}_{\text{FH}} \otimes \mathbf{E}_{\text{FH}})] d^3\mathbf{r} \right\}^2}_{\text{Nonlinear coupling}} \\
 & \times \left[\underbrace{Q_{\text{SH}} \kappa_{\text{SH}} L_{\text{SH}}(2\omega)}_{\text{SH out-coupling}} \right], \tag{9}
 \end{aligned}$$

where $L_0(\omega) = \gamma_0^2 / [(\omega - \omega_0)^2 + \gamma_0^2]$ represents the spectral overlap factor, κ_{FH} quantifies coupling of the incident wave to the FH mode, κ_{SH} quantifies coupling of the SH

eigenmode to the desired SH beam.

The most straightforward parameter to engineer is the quality factor of FH mode Q_{FH} (e.g., the losses of FH mode) to enhance the amplitude of intracavity FH field. On resonance, temporal coupled-mode theory gives the field enhancement¹⁷⁷:

$$\mathbf{E}_\omega / \mathbf{E}_{\text{inc}} \propto Q_{\text{FH}} \times \kappa_{\text{FH}} \propto \gamma_{\text{FH},r} / (\gamma_{\text{FH},r} + \gamma_{\text{FH,nr}})^2. \tag{10}$$

For the case that non-radiative loss is negligible ($\gamma_{\text{FH},r} \gg \gamma_{\text{FH,nr}}$), lowering radiation loss strengthens field confinement. More generally, the non-radiation loss and radiation loss are comparable, it is the critical couple ($\gamma_r = \gamma_{nr}$) that makes largest intracavity field enhancement. This operating point balances in-coupling efficiency with resonant field enhancement, yielding the largest enhancement.

The remaining two process (nonlinear and SH out-coupling), require engineering of the SH eigenmode, which ultimately determines the SHG beam properties (e.g., vortex, vector, or tightly focused beams). However, SH modes with tailored far-field properties usually exhibit high in-plane symmetric near field profile. If this profile is poorly matched to the EFISH polarization source, the desired SH beam will not be efficiently generated. Thus, considering the overlap integral between the EFISH source and the SH eigenmode is essential. With these considerations, we review recent advances in EFISH metasurfaces.

Cai et al.¹⁷⁸ first demonstrated EFISH enhancement using metallic plasmonic metagratings filled with nonlinear poly-methyl methacrylate (PMMA), as illustrated in Fig. 10(a). The metallic structures defined the optical cavity and served as electrodes connected to external circuits, enabling electrical control over fields within the nonlinear medium. They achieved a modulation depth of 7% V^{-1} and a conversion efficiency of 5.7×10^{-11} . A similar two-dimensional metallic metasurface (Fig. 10(b)), consisting of a 50 nm thick metal layer patterned with holes on a silver substrate separated by a 100 nm alumina dielectric layer, exhibited EFISH arising from the dielectric alumina and the metal-alumina interface. This configuration yielded a modulation depth of 9% V^{-1} and a conversion efficiency of 2×10^{-11} ¹⁷⁹. Furthermore, employing a hybrid plasmonic electrolyte system immersed in aqueous electrolyte solution significantly enhanced EFISH due to voltage-assisted charge accumulation, achieving an exceptional modulation depth of approximately 150% V^{-1} ¹⁸⁰. Beyond metallic structures, dielectric nanostructures offer strong optical confinement through Mie resonances¹⁸¹. Low losses and high damage thresholds make dielectric metasurfaces attractive for nonlinear optics, especially at high pump intensities. Dielectric metasurfaces composed of high-index unit cells support high-Q quasi-normal modes (QNMs) coupling to free space via multipole channels¹⁵⁷, enhancing harmonic generation efficiency through intensified light-matter interactions¹⁸². Kyu-Tae et al.¹⁸³ studied EFISH in a silicon grating leveraging magnetic Mie

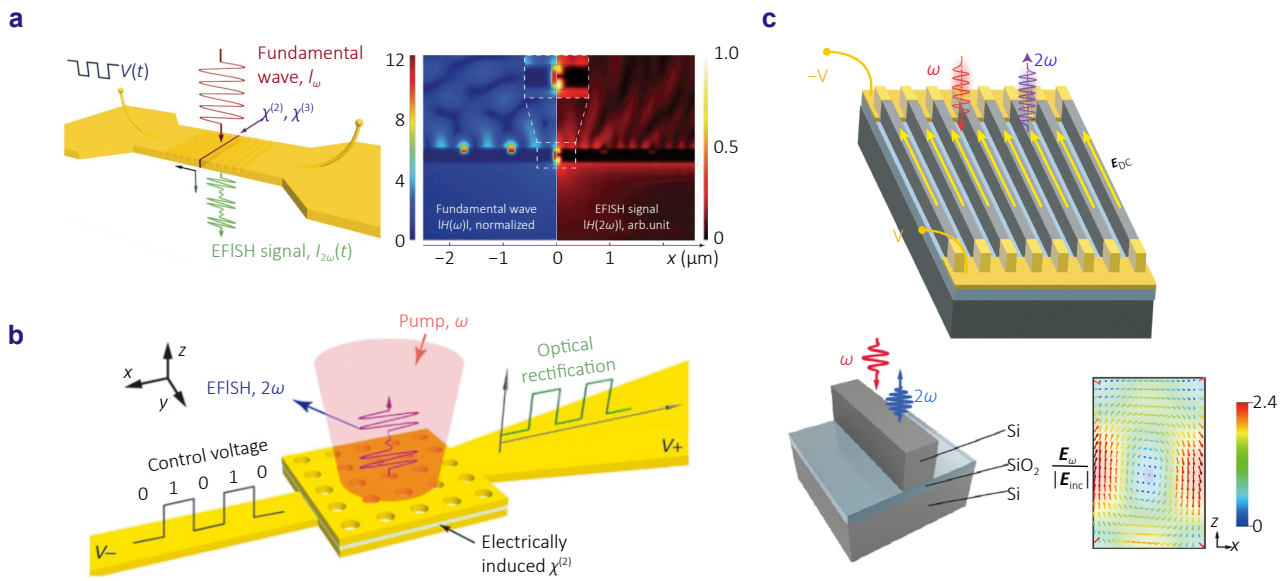


Fig. 10 | EFISH in metamaterials. (a) Schematic of a plasmonic EFISH device: a gold nanoslit resonator surrounded by a grating-based optical nanoantenna, with both metallic parts wire-bonded to external circuitry. The fundamental wave is localized in the plasmonic cavity so that EFISH signal is enhanced. (b) Schematic of a metasurface EFISH device: a 50 nm perforated gold film separated from an unpatterned silver layer by a 100 nm Al₂O₃ spacer. The hole array has a diameter of 186 nm and a square lattice period of 370 nm. Both metallic films serve as electrodes when connected to external circuitry. (c) Schematic of a Mie resonance EFISH device (upper), drawn based on ref.¹⁸³. Unit-cell schematic of a silicon metasurface with 2.4 fold field enhancement via MD resonance. Figure reproduced with permission from: (a) ref.¹⁷⁸, AAAS; (b) ref.¹⁷⁹, Springer Nature; (c) ref.¹⁸³, American Chemical Society.

resonances, with electrodes positioned on opposite sides (Fig. 10(c)). The fundamental electric field was confined within the silicon via an MD resonance, achieving a field enhancement factor of 2.4. Consequently, the SHG intensity experienced only a 1.2-fold enhancement under a 10 V external bias, corresponding to a modulation depth of approximately 1.2% V⁻¹.

Beyond Q_{FH} , several parameters in Eq. (9) remain underexplored, which outline the possible future research directions: (i) operating at critical coupling to maximize the field enhancement; (ii) co-localizing and shaping the E_{DC} , E_{FH} and E_{SH} to enhance the nonlinear overlap integral (e.g., spontaneous mode matching via CPE, co-design of electrical device structure and optical structure topology to confining both E_{DC} and E_{FH} in the same cavity); (iii) engineering the SH eigenmode and its radiation channel to control the emitted SH beam.

3 CISH and QCSE

The fundamentals of the distinction of EFISH with CISH and QCSE have been discussed in Section 2 in detail. Here we provide an overview of the state of the art of CISH and QCSE research to distinguish it from EFISH.

CISH, theoretically predicted by Khurgin¹⁸⁴ and experimentally validated by van Driel et al.^{111,144} in GaAs via simultaneous one- and two-photon interband absorption-induced currents. This phenomenon has been observed in several materials, including bilayer graphene (BLG)¹⁸⁵, silicon¹⁸⁶,

and GaAs³⁶ under various electrical configurations, such as optically induced currents and external electrode biases. For example, in a MSM device formed by depositing Au electrodes on a GaAs wafer³⁶ as illustrated in Fig. 11(a). The measured SHG power is proportional to the current density in agreement with Khurgin’s theoretical description¹⁸⁴. In AB-stacked graphene with an in-plane bias applied via a dual-gate FET¹⁸⁵, certain optical transitions are suppressed by a Fermi-level shift, thereby breaking the electron distribution symmetry in momentum space as illustrated in Fig. 11(b). In heavily doped silicon, earlier work¹⁸⁶ reported azimuthal anisotropy in SHG intensity similar to recent observations in graphene/SiO₂/Si(001) structures, where the dominant SHG contribution arises from EFISH induced by vertical electrostatic fields at silicon interfaces rather than purely momentum-space current-induced effects¹⁸⁷. This has prompted ongoing debate regarding the mechanisms responsible for CISH in different silicon devices.

Additionally, a unique type of current known as spin current which is characterized by opposite spin electron populations induces chiral CISH. Circularly polarized light prepares spin-selective carrier populations illustrated in Fig. 11(c), yielding a non-symmetric momentum-spin distribution that generates SH polarization dependent on the incident helicity²¹. Experimentally, this pure spin current can be all-optically injected into GaAs through quantum interference between one- and two-photon absorption pathways, causing electrons with opposite spins to populate states with opposite momenta^{144,188}. The generation of this pure spin

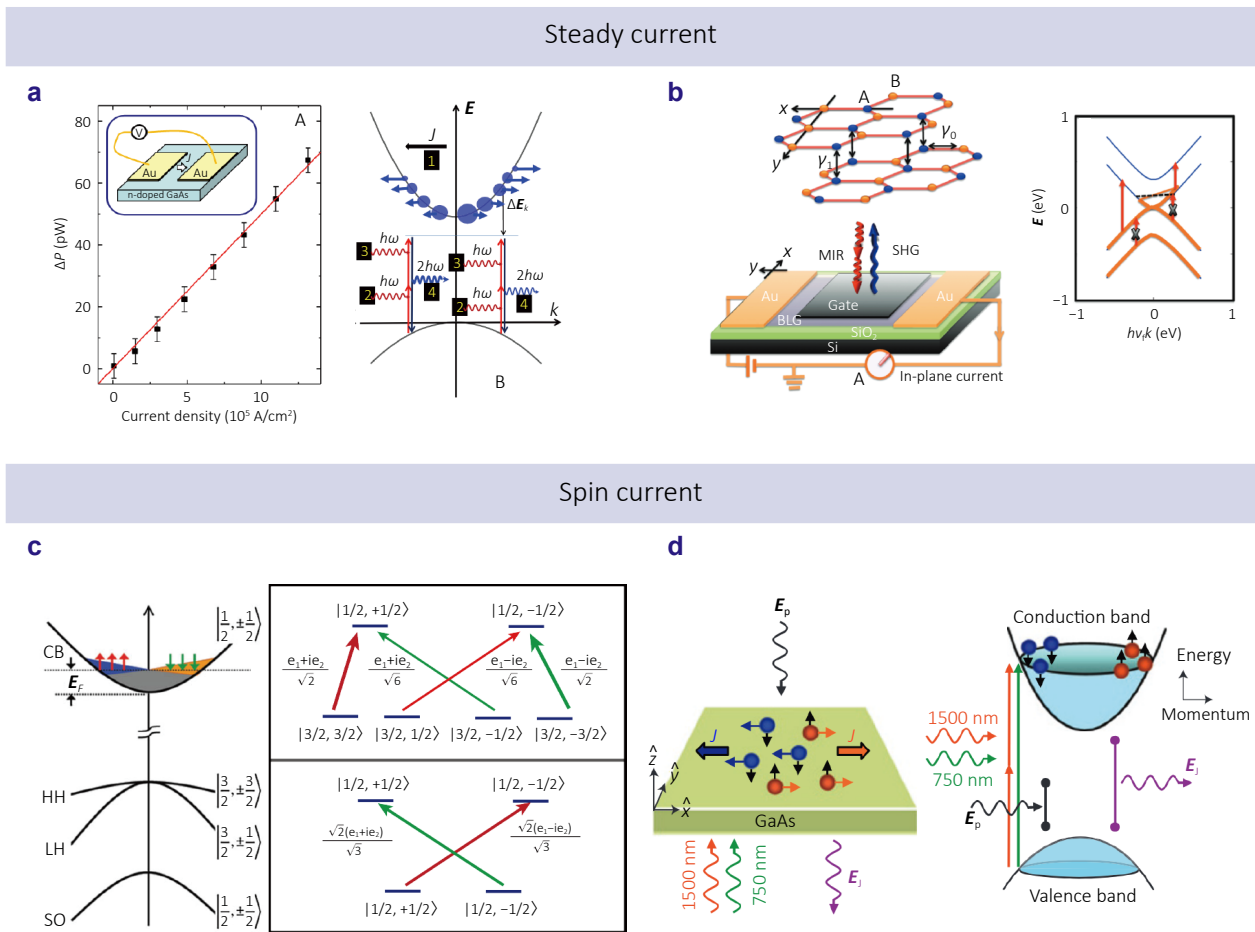


Fig. 11 | Current induced SHG steady current induced SHG. (a) The schematic of the device geometry. The SH power scales linear to the current density. Microscopically: (1) DC current arises from an asymmetric carrier distribution in k space; (2–3) virtual two-photon transitions driven by fundamental photons, with transition matrix elements incorporating electron momentum and detuning E_k ; (4) induced polarization at 2ω emits the SH photon. (b) (left top) Atomic structure of AB-stacked BLG with interlayer (γ_1) and intralayer (γ_0) hopping parameters and coordinate axes. (left bottom) The schematic of dual-gated bilayer graphene FET for CISH, with in-plane current along $-y$; Under bias, indicating Fermi level shifts includes symmetry broken. (c) Microscopic models for current induced sum-frequency susceptibility: full eight-band model showing the electron spin distribution with PSC and the relative dipole moments from the valence bands to the conduction band. (d) Experimental setup for observing spin-CISH in GaAs film. The GaAs sample is simultaneously illuminated by two laser pulses at 1550 nm and 750 nm. The interference between the transition pathways causes electrons with opposite spin orientations to be excited to energy states with opposite momenta (orange and blue spheres). As the two spin systems move along opposite directions, a pure spin current is formed. The nonlinear optical effect of the injected pure spin current is studied by detecting second-harmonic generation E_j from a probe pulse E_p . Figure reproduced with permission from: (a) ref.³⁶, American Physical Society; (b) ref.¹⁸⁵, American Chemical Society; (c) ref.²¹, American Physical Society; (d) ref.¹⁸⁹, Springer Nature.

current breaks the bulk centrosymmetry, enabling a probe field E_p to produce a chiral SHG signal E_j (Fig. 11(d))¹⁸⁹.

QCSE is typically observed in atomically thin layered materials. In contrast to the layer-dependent EFISH behavior in vdW material. QCSE in vdW materials is modeled as a uniform out-of-plane E_{DC} acting on layers with the layer-independent exciton dynamics. For example, the QCSE in monolayer and few-layer MoS₂²⁴ shows broadly similar behavior across different layers, indicating weak dependence on interlayer hybridization. By contrast, EFISH-like phenomena in bilayer MoS₂⁷⁸ exhibits substantial dependence on interlayer hybridization, as discussed in Section 2.1.2.

Another atomically scaled structure exhibiting strong nonlinearities is the Multiple Quantum Wells (MQW)³⁷, which can achieve nonlinearity 3 to 5 orders of magnitude higher than that of natural nonlinear crystals¹⁹⁰ and significant modulation depth through QCSE²². However, the nonlinear susceptibility tensor associated with intersubband transitions in MQWs is oriented exclusively along the growth direction, resulting in negligible nonlinear polarization for normally incident light¹⁹¹. Consequently, subsequent research has primarily focused on harnessing intersubband nonlinearities within waveguide geometries^{192,193}. Recently, integrating IST-driven $\chi_{eff}^{(2)}$ resonances in multiple

quantum wells with photonic modes in metasurfaces has emerged as a powerful approach for generating harmonic radiation from free-space excitation¹⁹⁴. By engineering the thicknesses of wells, MQW enable precise control over subband energies and transition dipole moments¹⁹⁵, resulting in highly resonant nonlinear susceptibilities^{193,195–197}. Lee et al. demonstrated a giant nonlinear response (54 nm/V) by combining quantum-electronic engineering of intersubband nonlinearities with electromagnetic engineering of L-shaped plasmonic nanoresonators, see Fig. 12(a, b)¹⁹⁴. Subsequent MQW metasurface architectures include all-dielectric bound-state-in-the-continuum designs¹⁹⁸, epsilon-near-zero structures¹⁹⁹, and intensity-saturation-mitigating geometries^{200,201}. Furthermore, the significant Stark shifts inherent to ISTs offer additional electrical tunability of $\chi^{(2)}$ ^{22,202}, establishing MQW metasurfaces as a versatile platform for voltage-controlled nonlinear photonics. Yu et al. designed a metasurface comprising MQW meta-atoms integrated with Au-plasmonic nanoantenna electrodes serving as bias contacts as illustrated in Fig. 12(c)²⁶. Under applied biases of

0, +4, and -4 V, the conduction-band profile of a single MQW period changes. Consequently, both the amplitude and phase of the effective second-order susceptibility $\chi_{\text{eff}}^{(2)}$ are electrically modulated, see Fig. 12(d). By carefully engineering the spatial distribution of the applied voltage, a corresponding spatial profile of $\chi_{\text{eff}}^{(2)}$ is realized, enabling dynamic control over nonlinear beam manipulations.

In conclusion, CISH is relevant in materials with high carrier densities where EFISH is suppressed, and QCSE arises in quantum-engineered, low-dimensional systems. While both mechanisms are well established at the physics level^{21,22}, device-scale engineering remains an open frontier. Recent demonstrations that combine QCSE with metasurfaces show electrically reconfigurable nonlinear beam steering²⁶, opening a promising route for applications. A key limitation, however, is the external electrodes that cannot independently address each meta-atom, constraining functionalities such as vortex-beam generation and dynamic focusing. Overcoming this will likely require per-pixel addressability to enable full spatial control.

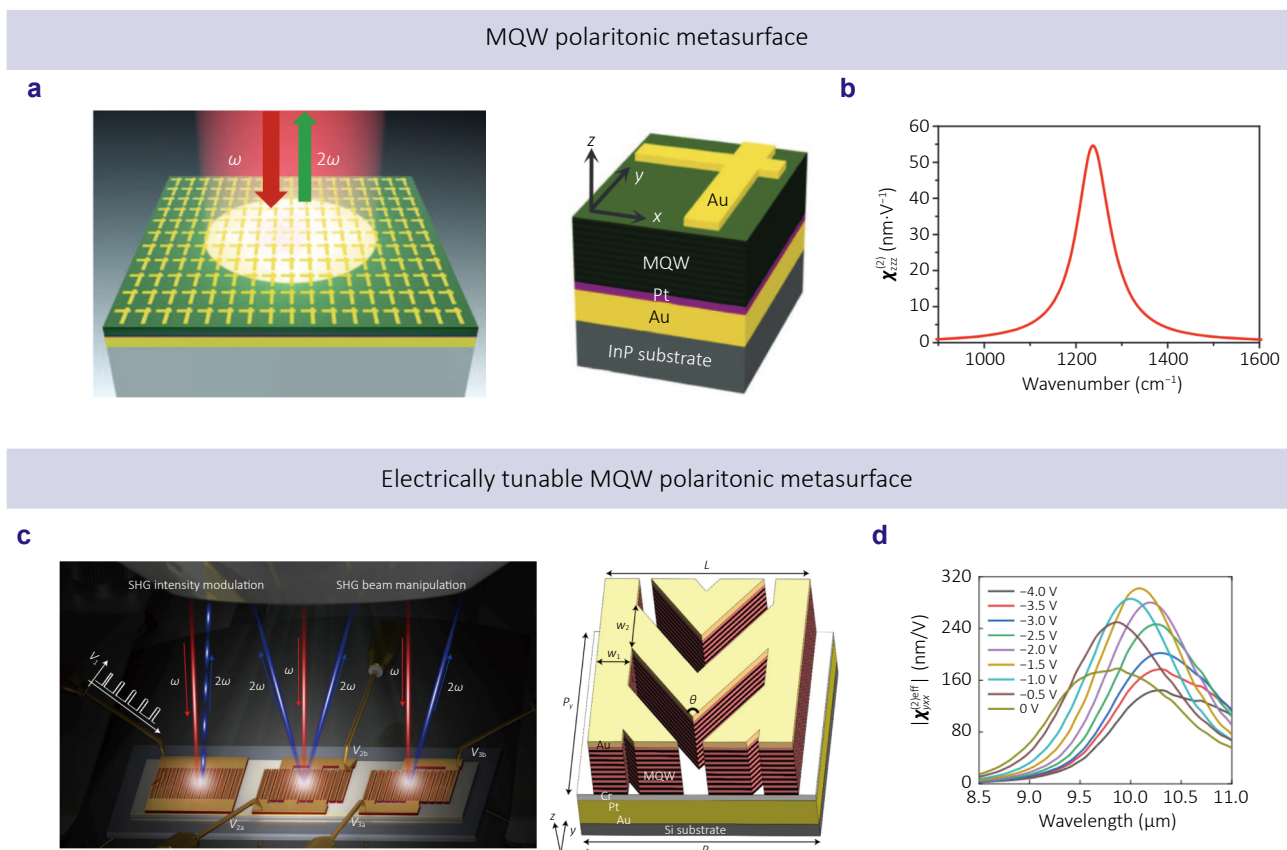


Fig. 12 | Electrically tunable nonlinear polaritonic metasurface for SHG. (a) Schematic of the metasurface design. (b) Intersubband nonlinear susceptibility of this MQW. (c) Operation modes of the electrically tunable metasurface: SHG intensity modulation (left), beam diffraction (center), and beam steering (right). And schematic of the meta-atom unit structure. (d) Calculated spectral dependence of the effective nonlinear susceptibility $\chi_{\text{eff},yxx}^{(2)}$ (V) for various bias voltages. Figure reproduced with permission from: (a, b) ref.¹⁹⁴, (c, d) ref.²⁶, Springer Nature.

4 Applications

4.1 Optical devices

In optics, EFISH enables second-order nonlinear optical responses in centrosymmetric materials by applying an electrostatic-field bias. Practical implementation have been discussed in Section 2.2 in detail. Specially, EFISH enables electrical control over the spatial modulation of $\chi_{\text{eff}}^{(2)}$, making it a highly promising effect for efficient and electrically tunable SHG. The performance metrics for second-harmonic generation across various material and structural configurations are comprehensively summarized in Table 1.

This table indicates that distinctive electronic characteristics yield very large modulation depths, while long interaction length with phase-matching enables high conversion efficiency. Although EFISH implementations on metasurfaces have so far underperformed on both metrics, their ability to manipulate free-space nonlinear beams remains compelling. Looking ahead, co-design of materials and on-chip device architectures that enable EFISH-driven phase matching could simultaneously realize large conversion efficiency and modulation depth. Moreover, EFISH-enabled mode matching between FH and SH in nano-device remains largely unexplored and represents a promising direction.

In addition to SHG, spatial modulation $\chi_{\text{eff}}^{(2)}$ by EFISH effect enables phase-matching conditions for other second-order nonlinear process. Thus provide new opportunities for integrated nonlinear photonic devices such as high-frequency laser^{203–205}, optical parametric amplification (OPA) waveguide and frequency-comb self-referencing^{206–208}. For example, OPA requires precise phase engineering of the pump, signal, and idler waves²⁰⁹. EFISH-induced periodic $\chi_{\text{eff}}^{(2)}$ gratings can arbitrarily engineer the momentum matching¹⁰³, as detailed in Section 2.2. Thus provide a promising platform for high performance OPA. Heydari et al.²¹⁰ employed this periodic modulation of the effective second-order susceptibility $\chi_{\text{eff}}^{(2)}$ in silicon waveguides by integrating alternating p–i–n diode arrays as illustrated in Fig. 13(a). This spatially varying bias profile enables quasi-phase-matched OPA directly on-chip. Under strong second-harmonic pumping at 1196 nm with a 31 V reverse bias, their device achieved phase-sensitive amplification at the fundamental wavelength, reaching a normalized gain of $0.6 \text{ dBW}^{-1/2} \text{ cm}^{-1}$.

While electrode design provides spatially uniform DC fields with high freedom, the complex manufacturing process limits its development. CPE offers an all-optical alternative by inscribing periodic DC-field-induced $\chi_{\text{eff}}^{(2)}$

Table 1 | Summary of electric-field-induced SHG system performance metrics.

Nonlinear material	Photonic structure	Electrical structure	Conversion efficiency (W^{-1})	Modulation depth (V^{-1})
Lead titanate/Strontium titanate ⁶²	Thin film	Metal electrode	9.3×10^{-11}	664%
Cadmium sulfide ⁵⁶	Nanobar	Metal electrode	4.4×10^{-9}	200%
Poly(9,9-di- <i>N</i> -dodecylfluorenyl-2,7-diyl) ²⁰	Thin film	Metal electrode	3.84×10^{-13}	422%
Molybdenum ditelluride ⁷⁴	Monolayer	Metal electrode	-	3000%
Molybdenum disulfide ⁷⁸	Bilayer	Metal electrode	-	200%
Rhenium disulfide ⁷⁶	Trilayers	Metal electrode	-	750%
Poly (methyl methacrylate) ¹⁷⁸	Metagrating	Metal electrode	7.5×10^{-15}	7%
Aluminum oxide ¹⁷⁹	Metasurface	Metal electrode	2.67×10^{-15}	9%
Gold/Potassium sulfate ¹⁸⁰	Metasurface	Hybrid metal-electrolyte	-	150%
Silicon ¹⁸³	Metagrating	Metal electrode	-	1.2%
Silicon ¹⁰³	Waveguide	p-i-n junction	0.13	-
Silicon ²¹⁰	Waveguide	p-i-n junction	0.114	-
Silicon nitride ¹³⁵	Waveguide	CPE	5×10^{-4}	-
Silicon nitride ¹³⁶	Waveguide	CPE	5×10^{-5}	-
Silicon nitride ^[251]	Waveguide	CPE	8×10^{-5}	-
Silicon nitride ¹⁴⁶	Waveguide	CPE	5×10^{-5}	-
Silicon nitride ¹⁴¹	Waveguide	CPE	3.1×10^{-3}	-
Silicon nitride ¹³⁷	Microring	CPE	25	-
Silicon nitride ¹³⁸	Microring	CPE	0.467	-
Silicon nitride ¹²³	Microring	CPE	2.8	-
Silicon nitride ²¹¹	Microring	CPE	0.4	-
Silicon nitride ²¹³	Microring	CPE	6.5	-

Note: the SHG response is quantified by the maximum normalized conversion efficiency η_{norm} , defined as $P_{2\omega}/(P_{\omega}^2)$ and $P_{2\omega}/(P_{\omega,p}^2)$ under continuous-wave and pulse laser excitation respectively, where $P_{\omega,p}$ denotes the peak power of the incident pulse. The modulation depth is defined as $\Delta I_{2\omega}(V)/[I_{2\omega}(V=0)]$.

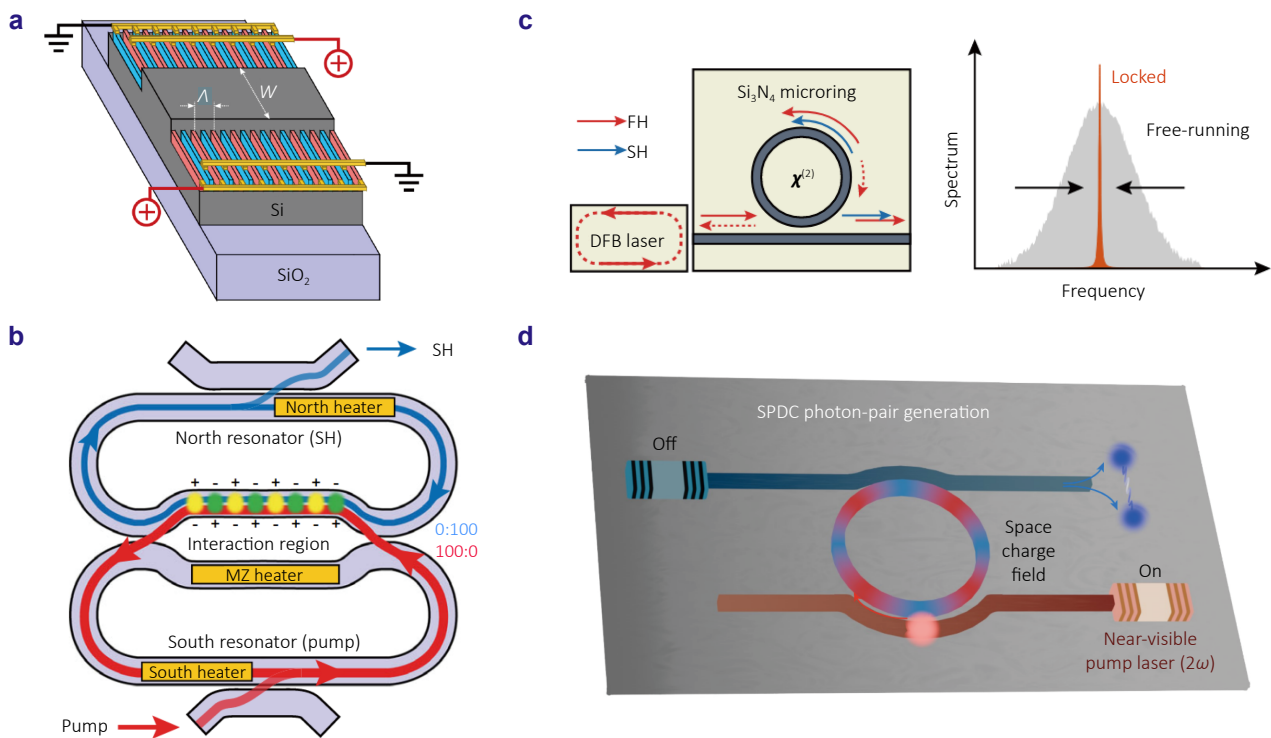


Fig. 13 | Integrated nonlinear photonic devices. (a) Silicon rib waveguides with alternating p-n diode sections and electrical bias points for field-induced nonlinear modulation. (b) Ultrabroadband milliwatt-level resonant frequency doubling on a chip. The pump and SH circulate respectively in the south and north loops, sharing a fraction of the optical path where CPE occur. Thus this device combine both high confinement of the ring with the broadband of the waveguide. (c) SIL SHG source: a DFB laser injects the FH into a ring-resonator (solid red arrow). Rayleigh backscattering (dashed arrows) feeds a fraction of the intracavity field back into the DFB cavity, dramatically narrowing the emission linewidth. This SIL FH inject into the Si₃N₄ ring generating a narrow linewidth SH via CPE. (d) SPDC in a Si₃N₄ microresonator via CPE. Figure reproduced with permission from: (a) ref.²¹⁰, Optica Publishing Group; (b) ref.²¹¹, under Creative Commons licences; (c) ref.²¹², (d) ref.²¹³, Springer Nature.

gratings directly into photonic structures such as straight waveguides and microring resonators satisfying the quasi-phase-matching condition spontaneously. Employing a dual-resonator CPE architecture, conversion efficiencies up to 2500% W^{-1} with milliwatt-level SHG output have been demonstrated¹³⁷. However, perfect phase matching is restricted to a single resonant mode so that the spectral range is limited, thereby constraining the usable spectral range. To address this, Marco et al.²¹¹ using separate race-track resonators for the FH and SH (the south and north rings in Fig. 13(b)), respectively. A Mach-Zehnder interferometer (MZI) with tunable thermal phase shifters decouples FH from north ring (achieving a 100 : 0 splitting ratio in the pump band) and SH entirely into the south ring (0 : 100). Both resonators were engineered to satisfy free spectral range (FSR) matching $FSR_{FH} \approx FSR_{SH}$, enabling multiple doubly resonant mode pairs across the QPM bandwidth. Within their shared waveguide segment, CPE inscribes a periodic DC-field-induced $\chi_{eff}^{(2)}$ grating that meets the QPM condition over more than 200 nm of the spectral range. As a result, this dual-resonator system generates broadband, milliwatt-level SHG in the North ring with 40% W^{-1}

conversion efficiency.

Additionally, Marco et al.²¹² integrated an electrically pumped distributed-feedback (DFB) laser with a Si₃N₄ microring resonator realizing a self-injection-locked (SIL) second-harmonic source with an ultranarrow emission linewidth as illustrated in Fig. 13(c). In their design, the DFB laser is edge-coupled into the microring, where CPE inscribes a DC-field-induced $\chi_{eff}^{(2)}$ grating in the fundamental transverse-electric TE₀₀ mode to achieve quasi-phase matching. Simultaneously, Rayleigh backscattering from sidewall roughness provides intrinsic optical feedback by recirculating a fraction of the microring field back into the laser cavity, suppressing phase noise by a factor proportional to Q^2 . Because the SIL-locked emission frequency coincides with the TE₀₀ resonance, the same inscribed $\chi_{eff}^{(2)}$ grating automatically satisfies the quasi-phase-matching condition for second-harmonic generation. This dual-function architecture combines SIL linewidth stabilization with on-chip EFISH-enabled strong sidemode suppression ratio exceeding 60 dB.

Recently, this preminent second-order nonlinearity property in Si₃N₄ microring resonators has been developed

for spontaneous parametric down-conversion (SPDC) as illustrated in Fig. 13(d). In the reported scheme, the fundamental transverse-electric mode at 1560 nm (chosen for optimal CPE) is pumped to inscribe a long-lived DC-field-induced $\chi_{\text{eff}}^{(2)}$ grating via CPE. Upon subsequent injection of a second-harmonic pump, this preexisting grating satisfies the QPM condition for SPDC. Resonant enhancement at down-conversion wavelength by the microring, together with the large FSR of the resonator, leads to entangled photon-pair generation rates up to 0.8 million pairs per second.

In conclusion, the key advantage of the EFISH in optical devices is the spatial programmability $\chi_{\text{eff}}^{(2)}(r)$, which relaxes otherwise stringent phase-matching constraints, especially, in materials that lack natural birefringence or domain inversion, thereby enabling QPM and a broad range of nonlinear on-chip functionality.

4.2 Carrier dynamics detection

Another application is time-resolved probing of carrier dynamics via the temporal EFISH response. The mechanism is that the different mobilities of electron and hole generate an electrostatic field that enables EFISH, as discussed in Section 2.2. Conversely, EFISH signals can serve as effective optical probes of carrier dynamics, a capability essential for both electronic^{214,215}, optoelectronic¹²⁵, and THz²¹⁶ devices.

4.2.1 Electron dynamic probing in electronic devices

Most electronic devices operate via the spatial transport of charge carriers. For example, FETs exploit carrier motion in a semiconductor channel that is modulated by an external gate voltage^{217–219}. In inorganic semiconductors, such as silicon^{220,221}, well-established experimental methods and physical models have promoted rapid advancements. Conversely, the underlying physics of organic²²² and ferroelectric⁴⁵ electronic devices remains less well understood, hindering performance optimization. Conventional scanning probe methods, such as scanning Kelvin probe microscopy and AFM-based potentiometry, provide high-resolution scalar potential mapping but lack direct measurement capabilities of vectorial electric fields. EFISH provides direct, non-invasive optical imaging of the in-plane vector electric field with approximately 0.5 μm spatial and 5 ns temporal resolutions²¹⁴. The coherent nature of SHG, highly sensitive to both the magnitude and orientation of static fields via the nonlinear susceptibility tensor, makes EFISH ideal for visualizing carrier injection, transport, and accumulation. Consequently, EFISH complements traditional scanning probe and charge modulation techniques by offering enhanced spatiotemporal resolution, critical for optimizing organic device performance^{223–225}. Furthermore, time-resolved EFISH offers direct insights into carrier dynamics, which are essential for improving device switching speeds,

reliability, and efficiency. For example, Xu et al.²²⁶ utilized time-resolved EFISH to study transient electric fields in ferroelectric barrier discharge (FBD) systems employing PZT electrodes. They observed field overshoots (approximately 13 kV/cm compared to 5 kV/cm in conventional discharges) and significantly prolonged plasma durations due to rapid ferroelectric polarization-induced surface charges, phenomena highly relevant for plasma catalysis and material synthesis.

4.2.2 Carrier dynamic probing in solar cells

In optoelectronic devices, carrier dynamics at ultrafast timescales are critically important. Unlike electrically driven carriers whose response is inherently limited by comparatively slow electrical modulation speeds, optically excited carrier respond on femtosecond timescales. Leveraging ultrafast spectroscopic techniques, EFISH can directly probe these ultrafast carrier dynamics with femtosecond temporal resolution. Specifically, in centrosymmetric semiconductors, time-resolved EFISH (TREFISH) effectively measures interfacial electric fields arising from ultrafast electron transfers, exhibiting exceptional sensitivity at crystalline interfaces due to the intrinsic bulk-forbidden SHG signal. Devizis et al.¹²⁵ first demonstrated TREFISH in conjugated polymer-based devices employing ITO electrodes, see Fig. 13(a), revealing charge relaxation dynamics within disordered organic solids. Subsequently, TREFISH became instrumental in studying photovoltaic mechanisms, notably within organic photovoltaics (OPVs)²²⁷ and hot-electron photovoltaic²²⁸ devices.

Typical photovoltaic processes include²²⁹: (i) photogeneration of hot electrons by photons whose energies exceed the semiconductor bandgap; (ii) rapid cooling resulting in exciton formation (electron-hole pairs bound by Coulomb attraction), necessitating subsequent separation at donor-acceptor interfaces; and (iii) charge transfer processes yielding free carriers. However, carrier dynamics in organic materials are inherently more complex, which limits the power-conversion efficiency of OPVs compared to their inorganic counterparts²³⁰. In 2013, Vithanage et al.²²⁷ utilized TREFISH to elucidate charge-separation mechanisms in bulk-heterojunction organic solar cells, revealing rapid spatial separation (several nanometers within picoseconds) of initially closely bound electron-hole pairs (< 1 nm). This rapid separation overcomes Coulombic attraction, generating free carriers within sub-nanosecond timescales, see Fig. 14(b). Insights from such studies guided the development of advanced electron-donor and electron-acceptor materials, including polymers and fullerenes. Conventionally, carrier mobilities in organic materials are treated as near-equilibrium constants determined by diverse measurement techniques. However, Melianas et al.²³¹, combining TREFISH experiments with kinetic Monte Carlo simulations, demonstrated significant time dependence in carrier mobility, see Fig. 14(c). Moreover, the inherently low dielectric constant

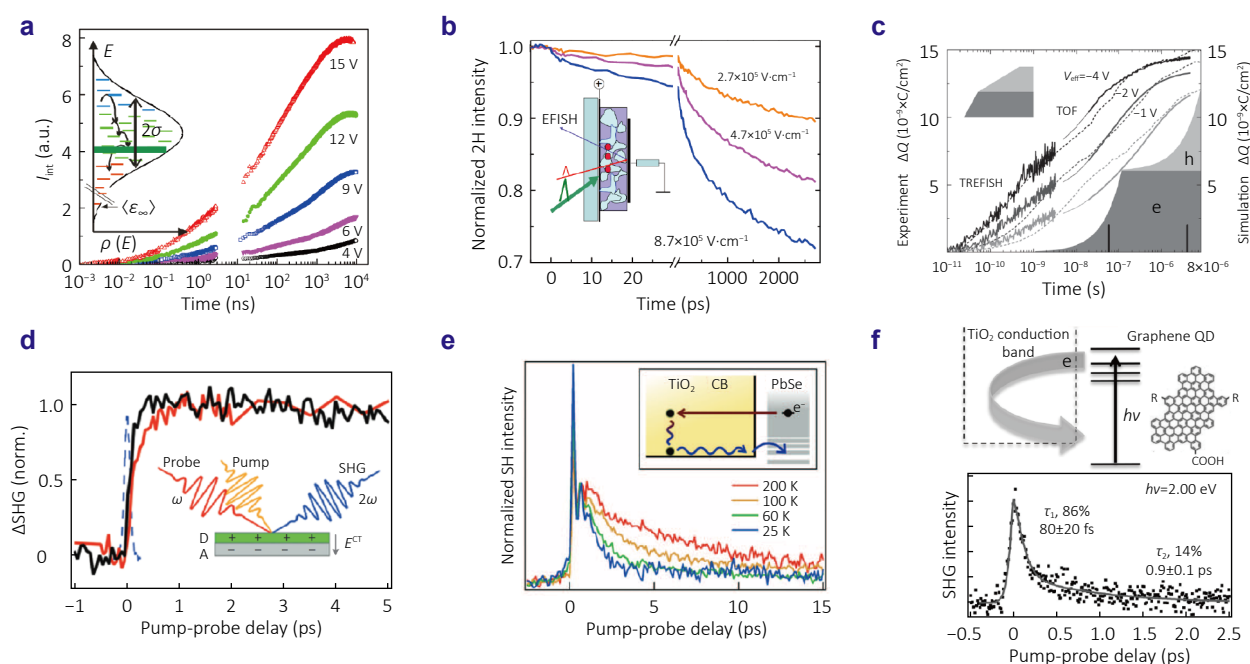


Fig. 14 | Time-resolved EFISH application in Photovoltaic. (a) Integrated photocurrent from TREFISH and time-of-flight (TOF) measurements at various applied voltages after subtracting the exciton contribution $E_{\text{exc}}(t)$. Inset: schematic density-of-states (DOS) in a disordered organic solid, showing the Gaussian DOS (width 2σ), equilibrium carrier energy E_{eq} , and transport energy (shaded bar). (b) Experimental kinetics of the second-harmonic intensity under different electric field strengths. (c) Combined TREFISH/TOF transients (solid lines) and Monte Carlo simulation results (dashed lines) at various effective biases. The initial ~ 20 ns (thinner lines) may be unreliable due to TOF limitations. Shaded regions indicate non-dispersive extraction, with mean extraction times of 0.06 (electrons) and 4 (holes) μs (vertical bars). Inset: same data on a linear time scale. Reproduced with permission²³¹. (d) TR-SHG spectra of donor/acceptor bilayers: 3 nm CuPc on 20 nm C₇₀ (red, $h\nu=2.03$ eV) and 3 nm CuPc on 20 nm C₆₀ (black, $h\nu=2.02$ eV). (e) Temperature-dependent decay of the pump-induced SHG enhancement (normalized to the initial change illustrating recovery rates). Inset: cartoon of ballistic electron injection (straight arrow), phonon scattering and polaron transport (wavy lines), and back-transfer to the nanocrystal (curved arrow). (f) Energy level diagram of the C132A graphene quantum dot on TiO₂(110): valence-band maximum and conduction-band minimum. TR-SHG spectra (dots) for 0.5 ML C132A/TiO₂ at 300 K with pump photon energies of 2.00 eV (lower). Solid lines are biexponential fits; shaded regions indicate fit uncertainty. Probe photon energy: 1.53 eV; detected SHG at 3.06 eV. Figure reproduced with permission from: (a) ref.¹²⁵, American Physical Society; (b) ref.²²⁷, Springer Nature; (c) ref.²³¹, John Wiley and Sons; (d) ref.²³², Springer Nature; (e) ref.²²⁸, AAAS; (f) ref.²³⁴, American Chemical Society.

of organic semiconductors intensifies electron-hole Coulomb interactions, complicating free-carrier generation. While the exact mechanism allowing electrons and holes to escape Coulombic trapping remains incompletely understood, mounting evidence highlights the critical role of hot charge-transfer (CT) excitons in facilitating free-carrier formation. Jailaubekov et al.²³² employed femtosecond EFISH measurements to directly visualize hot CT exciton formation and relaxation dynamics in OPVs, see Fig. 14(d).

Beyond traditional electron-hole pair separation, directly harvesting hot electrons before thermalization offers promising pathways for efficiency improvement. Typically, hot electrons rapidly lose energy through ultrafast relaxation processes. As previously discussed, hot-electron dynamics generated via LSPR in metallic structures can be probed through ultrafast EFISH signals¹³⁴. Analogously, EFISH is effective in examining hot-electron dynamics in semiconductor systems. One promising approach involves semiconductor nanocrystals or quantum dots (QDs)²³³,

where quantum confinement discretizes electronic energy bands. Such discretization often results in energy-level spacings greater than lattice phonon energies, creating a phonon bottleneck that significantly slows hot-electron relaxation via multiphonon processes. Tisdale et al.²²⁸ employed SHG signals to observe hot-electron transfer from colloidal PbSe nanocrystals to TiO₂, resolving transfer events on the order of ~ 50 fs, see Fig. 14(e). Similarly, Williams et al.²³⁴ investigated hot-electron transfer dynamics from graphene quantum dots to TiO₂, see Fig. 14(f). Their study identified two distinct decay pathways: (1) rapid recombination of interfacial electron-hole pairs occurring within the initial 15 fs, and (2) a slower, temperature- and excitation-energy-dependent relaxation pathway termed the boomerang mechanism. In the latter mechanism, hot electrons injected into bulk TiO₂ undergo cooling via electron-phonon interactions, then drift back toward the interface under transient electric fields, recombining with holes on the graphene quantum dots within approximately 2 ps.

4.2.3 Electron dynamic probing of THz response

Another intriguing area of research involves the material response at terahertz (THz) frequencies, situated between the microwave and optical regimes. Unlike dipoles generated by electron-cloud distortion with optical incident or steady-state carrier drift described typically by current-voltage (I - V) characteristics, the THz response is dominated by ultrafast displacement of free or weakly bound carriers³³⁵. Therefore, the electromagnetic response of materials at THz frequencies is typically characterized by the frequency-dependent permittivity, which describes the polarization induced by carrier motion. In most materials studied so far, carriers drift symmetrically along the direction of the incident THz electric field, resulting in nonlinear optical responses predominantly described by odd-order nonlinear

susceptibilities. Lee et al.²¹⁶ demonstrated that this symmetry can be broken through EFISH. The author engineer a GaAs structure with interdigitated electrodes. An incident optical pump excited electrons from the valence band to the conduction band, while intervalley scattering in doped GaAs provided large third-order nonlinear optical response at THz frequencies³³⁶. The external bias field, applied via these comb-like electrodes, disrupted the symmetry of photocarrier diffusion. Consequently, under optical excitation, this induced asymmetry in carrier distribution produced an observable THz EFISH signal, see Fig. 15(a).

In addition to driving carrier transport, intense THz radiation can also induce polarization switching in ferroelectric materials via resonant control over ionic motion as well as lattice vibrations. As previously discussed in Section 2.1,

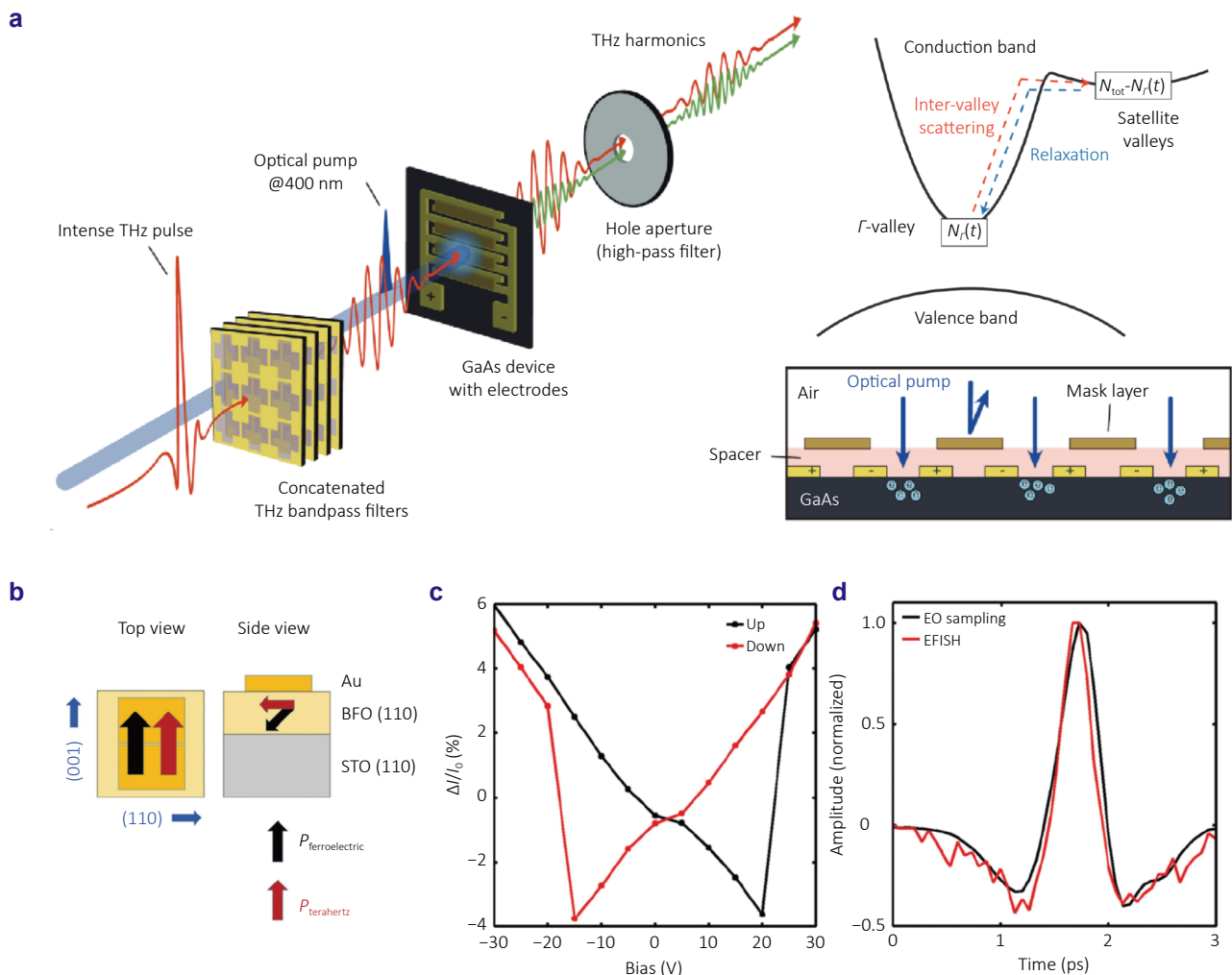


Fig. 15 | THz application (a) Schematic of device and experimental setup. Schematic diagram of the band structure of GaAs and the intervalley scattering. In this diagram, $N_r(t)$ and N_{tot} denote the electron concentration in the Γ -valley and total electron concentration in the conduction band, respectively. (b) Schematic showing sample electrode structure with incident THz pump pulse. (c) DC electrical biasing measurements with bias applied parallel to the ferroelectric polarization for a $2 \mu\text{m}$ gap on 60 nm BFO film showing butterfly switching loop and switching fields on the order of 100 kV/cm. (d) Low field THz EFISH measurement on the same BFO film shown in comparison to measured applied electric field profile measured by electro-optic sampling. Figure reproduced with permission from: (a) ref.²¹⁶, (b) ref.²³⁷, John Wiley and Sons.

polarization-state switching induced by external bias fields strongly modulates SHG⁵¹. EFISH can similarly serve as an optical probe to investigate optically induced ultrafast polarization-switching dynamics in ferroelectrics. Chen et al.²³⁷ employed EFISH to probe these ultrafast dynamics. They fabricated EO devices incorporating interdigitated electrode structures as illustrated in Fig. 15(b) and recorded the SHG signal under 800 nm optical excitation. Figure 15(c) shows the SHG response of a BiFeO₃ thin film within this EO structure. At low bias fields, the SHG intensity exhibits the characteristic EFISH modulation; when the applied field exceeds the known coercive field, pronounced butterfly loops appear, indicating full ferroelectric polarization switching, coincident with the recent result⁵¹. Moreover, by driving the film with single-cycle THz pulses, they generated transient electric fields on a sub-picosecond timescale, thereby modulating the polarization state. For small incident THz fields, the measured EFISH modulation has the same temporal dependence as measured by electro-optic sampling (Fig. 15(d)), indicating that the low-field THz drives an adiabatic, reversible tilt of the polarization vector rather than a hysteretic, permanent switching.

5 Summary and outlook

As demonstrated above, EFISH transcends the inherent symmetry limitations of traditional nonlinear materials, opening new avenues for applications across electrical²¹⁵, optical²¹³, optoelectronic²³⁸, and terahertz²¹⁶ devices. Recent pioneering work in material synthesis and structural engineering has demonstrated that the distortion of electron clouds under electrostatic fields, coupled with electron-based quasiparticles such as skyrmions⁶², excitons⁷⁸, and plasmons²³⁹, can dramatically enhance the EFISH response. The photonic structure design including both on-chip localized¹³⁷ and resonant leaky photonic states¹⁷⁸ have also shown superior performance in EFISH. A central challenge, however, is balancing conversion efficiency with modulation depth. Many materials exhibit high field sensitivity. However, the usable interaction length is limited by the requirement of phase matching. Most on-chip device research exhibits high conversion efficiency leveraging CPE, however, without dynamic electrical tunability.

Looking forward, materials research may target not only large EFISH modulation amplitudes but also tensor symmetry and bias orientation. Identifying crystals whose $\chi^{(3)}$ symmetry align with externally applied fields so that birefringent phase-matching conditions can be satisfied promises simultaneous gains in efficiency and tunability. On the device side, EFISH functionality could extend beyond simple SHG intensity modulation to a broader class of reconfigurable nonlinear photonic components. For example, pixel-level biasing of metasurfaces can spatially program $\chi_{\text{eff}}^{(2)}(r)$ enabling electrically tunable SHG encompassing

beam steering, vortex-beam generation, and polarization manipulation. We believe that the evolving landscape of the EFISH research not only broadens our fundamental understanding of light-matter interaction but also paves the way for innovative optoelectronics applications. Continued advancements in integrated photonic and electronic design will advance this transformative technology.

References

1. Boyd R W. *Nonlinear Optics* 4th ed (Elsevier, San Diego, 2020).
2. Franken PA, Hill AE, Peters CW et al. Generation of optical harmonics. *Phys Rev Lett* 7, 118–119 (1961).
3. Armstrong JA, Bloembergen N, Ducuing J et al. Interactions between light waves in a nonlinear dielectric. *Phys Rev* 127, 1918–1939 (1962).
4. Bloembergen N, Pershan PS. Light waves at the boundary of nonlinear media. *Phys Rev* 128, 606–622 (1962).
5. Zhang S, Liu L, Ren S et al. Recent advances in nonlinear optics for bio-imaging applications. *Opto-Electronic Adv* 3, 200003 (2020).
6. Kruk S S, Wang L, Sain B et al. Asymmetric parametric generation of images with nonlinear dielectric metasurfaces. *Nature Photonics* 16, 561–565 (2022).
7. Yanagimoto R, Ash BA, Sohoni MM et al. Programmable on-chip nonlinear photonics. *Nature* (2025). doi: [10.1038/s41586-025-09620-9](https://doi.org/10.1038/s41586-025-09620-9).
8. Boes A, Chang L, Langrock C et al. Lithium niobate photonics: unlocking the electromagnetic spectrum. *Science* 379, eabj4396 (2023).
9. Wang YF, Pan ZY, Yan YX et al. A review of gallium phosphide nanophotonics towards omnipotent nonlinear devices. *Nanophotonics* 13, 3207–3252 (2024).
10. Choy MM, Byer RL. Accurate second-order susceptibility measurements of visible and infrared nonlinear crystals. *Phys Rev B* 14, 1693–1706 (1976).
11. Schneider K, Welter P, Baumgartner Y et al. Gallium phosphide-on-silicon dioxide photonic devices. *J Lightw Technol* 36, 2994–3002 (2018).
12. Guyot-Sionnest P, Chen W, Shen YR. General considerations on optical second-harmonic generation from surfaces and interfaces. *Phys Rev B* 33, 8254–8263 (1986).
13. Jacobsen RS, Andersen KN, Borel PI et al. Strained silicon as a new electro-optic material. *Nature* 441, 199–202 (2006).
14. Cazzanelli M, Bianco F, Borga E et al. Second-harmonic generation in silicon waveguides strained by silicon nitride. *Nat Mater* 11, 148–154 (2012).
15. Schriever C, Bianco F, Cazzanelli M et al. Second-order optical nonlinearity in silicon waveguides: inhomogeneous stress and interfaces. *Adv Opt Mater* 3, 129–136 (2015).
16. Zhao Y, Jia WH, Wang XJ et al. Second-harmonic generation in strained silicon metasurfaces. *Adv Photonics Res* 3, 2200157 (2022).
17. Terhune RW, Maker PD, Savage CM. Optical harmonic generation in calcite. *Phys Rev Lett* 8, 404–406 (1962).
18. Soref R, Bennett B. Electrooptical effects in silicon. *IEEE J Quant Electron* 23, 123–129 (1987).
19. Kang L, Wu YH, Werner DH. Nonlinear chiral metasurfaces based on the optical kerr effect. *Adv Opt Mater* 11, 2202658 (2023).
20. Chen SM, Li KF, Li GX et al. Gigantic electric-field-induced second harmonic generation from an organic conjugated polymer enhanced by a band-edge effect. *Light Sci Appl* 8, 17 (2019).
21. Wang J, Zhu BF, Liu RB. Second-order nonlinear optical effects of spin currents. *Phys Rev Lett* 104, 256601 (2010).

22. Capasso F, Sirtori C, Cho AY. Coupled quantum well semiconductors with giant electric field tunable nonlinear optical properties in the infrared. *IEEE J Quant Electron* **30**, 1313–1326 (1994).
23. Dai YY, Wang YD, Das S et al. Electrical control of interband resonant nonlinear optics in monolayer MoS₂. *ACS Nano* **14**, 8442–8448 (2020).
24. Klein J, Wierzbowski J, Regler A et al. Stark effect spectroscopy of mono- and few-layer MoS₂. *Nano Lett* **16**, 1554–1559 (2016).
25. Chung H, Hwang I, Yu J et al. Electrical phase modulation based on mid-infrared intersubband polaritonic metasurfaces. *Adv Sci* **10**, 2207520 (2023).
26. Yu J, Park S, Hwang I et al. Electrically tunable nonlinear polaritonic metasurface. *Nat Photonics* **16**, 72–78 (2022).
27. Celebrano M, Wu XF, Baselli M et al. Mode matching in multiresonant plasmonic nanoantennas for enhanced second harmonic generation. *Nat Nanotechnol* **10**, 412–417 (2015).
28. Koshelev K, Kruk S, Melik-Gaykazyan E et al. Subwavelength dielectric resonators for nonlinear nanophotonics. *Science* **367**, 288–292 (2020).
29. Minkov M, Gerace D, Fan SH. Doubly resonant $\chi^{(2)}$ nonlinear photonic crystal cavity based on a bound state in the continuum. *Optica* **6**, 1039–1045 (2019).
30. Keren-Zur S, Michaeli L, Suchowski H et al. Shaping light with nonlinear metasurfaces. *Adv Opt Photonics* **10**, 309–353 (2018).
31. Sain B, Meier C, Zentgraf T. Nonlinear optics in all-dielectric nanoantennas and metasurfaces: a review. *Adv Photonics* **1**, 024002 (2019).
32. Frizyuk K. Second-harmonic generation in dielectric nanoparticles with different symmetries. *J Opt Soc Am B* **36**, F32–F37 (2019).
33. Khan AR, Zhang LL, Ishfaq K et al. Optical harmonic generation in 2D materials. *Adv Funct Mater* **32**, 2105259 (2022).
34. Cazzanelli M, Schilling J. Second order optical nonlinearity in silicon by symmetry breaking. *Appl Phys Rev* **3**, 011104 (2016).
35. Gigli C, Leo G. All-dielectric $\chi^{(2)}$ metasurfaces: recent progress. *Opto-Electron Adv* **5**, 210093 (2022).
36. Ruzicka BA, Werake LK, Xu GW et al. Second-harmonic generation induced by electric currents in GaAs. *Phys Rev Lett* **108**, 077403 (2012).
37. Gurnick M, DeTemple T. Synthetic nonlinear semiconductors. *IEEE J Quant Electron* **19**, 791–794 (1983).
38. Bavli R, Band YB. Relationship between second-harmonic generation and electric-field-induced second-harmonic generation. *Phys Rev A* **43**, 507–514 (1991).
39. Kittel C, McEuen P. *Introduction to Solid State Physics* (Wiley, Hoboken, 2018).
40. Ellinger S, Graham KR, Shi PJ et al. Donor-acceptor-donor-based π -conjugated oligomers for nonlinear optics and near-IR emission. *Chem Mater* **23**, 3805–3817 (2011).
41. Huang WJ, Xiao Y, Xia FF et al. Second harmonic generation control in 2D layered materials: status and outlook. *Adv Funct Mater* **34**, 2310726 (2024).
42. Vanderbilt D. *Berry Phases in Electronic Structure Theory: Electric Polarization, Orbital Magnetization and Topological Insulators* (Cambridge University Press, Cambridge, 2018).
43. Martin LW, Rappe AM. Thin-film ferroelectric materials and their applications. *Nat Rev Mater* **2**, 16087 (2017).
44. Zhang Y, Jie WJ, Chen P et al. Ferroelectric and piezoelectric effects on the optical process in advanced materials and devices. *Adv Mater* **30**, 1707007 (2018).
45. Khan AI, Keshavarzi A, Datta S. The future of ferroelectric field-effect transistor technology. *Nat Electron* **3**, 588–597 (2020).
46. Fiore A, Berger V, Rosencher E et al. Phase matching using an isotropic nonlinear optical material. *Nature* **391**, 463–466 (1998).
47. Kingon AI, Srinivasan S. Lead zirconate titanate thin films directly on copper electrodes for ferroelectric, dielectric and piezoelectric applications. *Nat Mater* **4**, 233–237 (2005).
48. Silva JPB, Silva JMB, Oliveira MJS et al. High-performance ferroelectric–dielectric multilayered thin films for energy storage capacitors. *Adv Funct Mater* **29**, 1807196 (2019).
49. Denev SA, Lummen TTA, Barnes E et al. Probing ferroelectrics using optical second harmonic generation. *J Am Ceram Soc* **94**, 2699–2727 (2011).
50. Abdelwahab I, Tilmann B, Wu YZ et al. Giant second-harmonic generation in ferroelectric NbO₁₂. *Nat Photonics* **16**, 644–650 (2022).
51. Feutmba GF, Hermans A, George JP et al. Reversible and tunable second-order nonlinear optical susceptibility in PZT thin films for integrated optics. *Adv Opt Mater* **9**, 2100149 (2021).
52. Xu B, Gong ZP, Liu JR et al. Tunable ferroelectric topological defects on 2D Topological surfaces: complex strain engineering skyrmion-like polar structures in 2D materials. *Adv Funct Mater* **34**, 2311599 (2024).
53. Junquera J, Nahas Y, Prokhorenko S et al. Topological phases in polar oxide nanostructures. *Rev Mod Phys* **95**, 025001 (2023).
54. Chen SQ, Yuan S, Hou ZP et al. Recent progress on topological structures in ferroic thin films and heterostructures. *Adv Mater* **33**, 2000857 (2021).
55. Han L, Addiego C, Prokhorenko S et al. High-density switchable skyrmion-like polar nanodomains integrated on silicon. *Nature* **603**, 63–67 (2022).
56. Rusu D, Peters JJP, Hase TPA et al. Ferroelectric incommensurate spin crystals. *Nature* **602**, 240–244 (2022).
57. Wang YJ, Feng YP, Zhu YL et al. Polar meron lattice in strained oxide ferroelectrics. *Nat Mater* **19**, 881–886 (2020).
58. Das S, Tang YL, Hong Z et al. Observation of room-temperature polar skyrmions. *Nature* **568**, 368–372 (2019).
59. Li Q, Nelson CT, Hsu SL et al. Quantification of flexoelectricity in PbTiO₃/SrTiO₃ superlattice polar vortices using machine learning and phase-field modeling. *Nat Commun* **8**, 1468 (2017).
60. Yadav AK, Nelson CT, Hsu SL et al. Observation of polar vortices in oxide superlattices. *Nature* **530**, 198–201 (2016).
61. Tang YL, Zhu YL, Ma XL et al. Observation of a periodic array of flux-closure quadrants in strained ferroelectric PbTiO₃ films. *Science* **348**, 547–551 (2015).
62. Wang SX, Li W, Deng CG et al. Giant electric field-induced second harmonic generation in polar skyrmions. *Nat Commun* **15**, 1374 (2024).
63. Wang Z, Sreekanth KV, Zhao M et al. Two-dimensional materials for tunable and nonlinear metaoptics. *Adv Photonics* **6**, 034001 (2024).
64. Du LJ, Hasan T, Castellanos-Gomez A et al. Engineering symmetry breaking in 2D layered materials. *Nat Rev Phys* **3**, 193–206 (2021).
65. Li YL, Rao Y, Mak KF et al. PRObing symmetry properties of few-layer MoS₂ and h-BN by optical second-harmonic generation. *Nano Lett* **13**, 3329–3333 (2013).
66. Yao KY, Finney NR, Zhang J et al. Enhanced tunable second harmonic generation from twistable interfaces and vertical superlattices in boron nitride homostructures. *Sci Adv* **7**, eabe8691 (2021).
67. Alexeev EM, Ruiz-Tijerina DA, Danovich M et al. Resonantly hybridized excitons in moiré superlattices in van der Waals heterostructures. *Nature* **567**, 81–86 (2019).
68. Ullah K, Meng YF, Shi Y et al. Harmonic generation in low-dimensional materials. *Adv Opt Mater* **10**, 2101860 (2022).
69. Shan YW, Li YG, Huang D et al. Stacking symmetry governed second harmonic generation in graphene trilayers. *Sci Adv* **4**, eaat0074 (2018).
70. Wang SX, Cui XH, Jian CE et al. Stacking-engineered heterostruc-

- tures in transition metal dichalcogenides. *Adv Mater* **33**, 2005735 (2021).
71. Geim AK, Grigorieva IV. Van der Waals heterostructures. *Nature* **499**, 419–425 (2013).
 72. Novoselov KS, Mishchenko A, Carvalho A et al. 2D materials and van der Waals heterostructures. *Science* **353**, aac9439 (2016).
 73. Brun SJ, Pedersen TG. Intense and tunable second-harmonic generation in biased bilayer graphene. *Phys Rev B* **91**, 205405 (2015).
 74. Wang Y, Xiao J, Chung TF et al. Direct electrical modulation of second-order optical susceptibility via phase transitions. *Nat Electron* **4**, 725–730 (2021).
 75. Yu HK, Talukdar D, Xu WG et al. Charge-induced second-harmonic generation in bilayer WSe₂. *Nano Lett* **15**, 5653–5657 (2015).
 76. Wang J, Han NN, Luo ZD et al. Electrically tunable second harmonic generation in atomically thin ReS₂. *ACS Nano* **16**, 6404–6413 (2022).
 77. Cha S, Ouyang TY, Taniguchi T et al. Enhancing resonant second-harmonic generation in bilayer WSe₂ by layer-dependent exciton-polaron effect. *Nano Lett* **24**, 14847–14853 (2024).
 78. Klein J, Wierzbowski J, Steinhoff A et al. Electric-field switchable second-harmonic generation in bilayer MoS₂ by inversion symmetry breaking. *Nano Lett* **17**, 392–398 (2017).
 79. Okada D, Araoka F. Electric-field-induced giant resonant enhancement of second harmonic generation in two-dimensional hybrid perovskite. *J Am Chem Soc* **147**, 14677–14683 (2025).
 80. Wang H, Qian XF. Giant optical second harmonic generation in two-dimensional multiferroics. *Nano Lett* **17**, 5027–5034 (2017).
 81. Feng W, Zheng W, Cao WW et al. Back gated multilayer InSe transistors with enhanced carrier mobilities via the suppression of carrier scattering from a dielectric interface. *Adv Mater* **26**, 6587–6593 (2014).
 82. Ho CH, Chu YJ. Bending photoluminescence and surface photovoltaic effect on multilayer InSe 2D microplate crystals. *Adv Opt Mater* **3**, 1750–1758 (2015).
 83. Ghosh S, Mishra MK, Kadambi SB et al. Designing elastic organic crystals: highly flexible polyhalogenated *N*-benzylideneanilines. *Angew Chem Int Ed* **54**, 2674–2678 (2015).
 84. Hao QY, Yi H, Su HM et al. Phase identification and strong second harmonic generation in pure ϵ -InSe and its alloys. *Nano Lett* **19**, 2634–2640 (2019).
 85. Wu MH, Zeng XC. Intrinsic ferroelasticity and/or multiferroicity in two-dimensional phosphorene and phosphorene analogues. *Nano Lett* **16**, 3236–3241 (2016).
 86. Chang K, Kaloni KP, Lin HC et al. Enhanced spontaneous polarization in ultrathin SnTe films with layered antipolar structure. *Adv Mater* **31**, 1804428 (2019).
 87. Singer KD, Sohn JE, Lalama SJ. Second harmonic generation in poled polymer films. *Appl Phys Lett* **49**, 248–250 (1986).
 88. Clark HA, Campagnola PJ, Wuskell JP et al. Second harmonic generation properties of fluorescent polymer-encapsulated gold nanoparticles. *J Am Chem Soc* **122**, 10234–10235 (2000).
 89. Delaire JA, Nakatani K. Linear and nonlinear optical properties of photochromic molecules and materials. *Chem Rev* **100**, 1817–1846 (2000).
 90. Cho MJ, Choi DH, Sullivan PA et al. Recent progress in second-order nonlinear optical polymers and dendrimers. *Prog Polym Sci* **33**, 1013–1058 (2008).
 91. Ju JJ, Kim J, Do JY et al. Second-harmonic generation in periodically poled nonlinear polymer waveguides. *Opt Lett* **29**, 89–91 (2004).
 92. Yap BK, Xia RD, Campoy-Quiles M et al. Simultaneous optimization of charge-carrier mobility and optical gain in semiconducting polymer films. *Nat Mater* **7**, 376–380 (2008).
 93. Kong JA. *Theory of Electromagnetic Waves* (Wiley, New York, 1975).
 94. Devreese JT, Camp P. *Electronic Structure, Dynamics, and Quantum Structural Properties of Condensed Matter* (Springer, New York, 1985).
 95. Widhalm A, Golla C, Weber N et al. Electric-field-induced second harmonic generation in silicon dioxide. *Opt Express* **30**, 4867–4874 (2022).
 96. Ren ML, Berger JS, Liu WJ et al. Strong modulation of second-harmonic generation with very large contrast in semiconducting CdS via high-field domain. *Nat Commun* **9**, 186 (2018).
 97. Böer KW. *Introduction to Space Charge Effects in Semiconductors* (Springer, Berlin Heidelberg, 2010).
 98. Akstipetrov OA, Fedyanin AA, Golovkina VN et al. Optical second-harmonic generation induced by a dc electric field at the Si-SiO₂ interface. *Opt Lett* **19**, 1450–1452 (1994).
 99. Akstipetrov OA, Fedyanin AA, Mishina ED et al. Dc-electric-field-induced second-harmonic generation in Si(111)-SiO₂-Cr metal-oxide-semiconductor structures. *Phys Rev B* **54**, 1825–1832 (1996).
 100. Gunn JB. Microwave oscillations of current in III–V semiconductors. *Solid State Commun* **1**, 88–91 (1963).
 101. Böer KW. Layer-like field inhomogeneities in homogeneous semiconductors in the range of "N-shaped negative differential conductivity". *Phys Rev* **139**, A1949–A1959 (1965).
 102. Böer KW, Voss P. Stationary high-field domains in the range of negative differential conductivity in cds single crystals. *Phys Rev* **171**, 899–903 (1968).
 103. Timurdogan E, Poulton CV, Byrd MJ et al. Electric field-induced second-order nonlinear optical effects in silicon waveguides. *Nat Photonics* **11**, 200–206 (2017).
 104. Jašinškas V, Gedvilas M, Račiukaitis G et al. Background-free electric field-induced second harmonic generation with interdigitated combs of electrodes. *Opt Lett* **41**, 2759–2762 (2016).
 105. Wagner KW. Erklärung der dielektrischen nachwirkungsvorgänge auf grund maxwellscher vorstellungen. *Arch Elektrotech* **2**, 371–387 (1914).
 106. Scherbak S, Reshetov I, Zhurikhina V et al. Maxwell-Wagner effect and second harmonic generation in gradient structures. *J Am Ceram Soc* **107**, 5569–5577 (2024).
 107. Bloch J, Mihaychuk JG, van Driel HM. Electron photoinjection from silicon to ultrathin SiO₂ films via ambient oxygen. *Phys Rev Lett* **77**, 920–923 (1996).
 108. Mihaychuk JG, Bloch J, Liu Y et al. Time-dependent second-harmonic generation from the Si-SiO₂ interface induced by charge transfer. *Opt Lett* **20**, 2063–2065 (1995).
 109. Österberg U, Margulis W. Dye laser pumped by Nd: YAG laser pulses frequency doubled in a glass optical fiber. *Opt Lett* **11**, 516–518 (1986).
 110. Dianov EM, Starodubov DS. Photoinduced generation of the second harmonic in centrosymmetric media. *Quantum Electron* **25**, 395–407 (1995).
 111. Atanasov R, Haché A, Hughes JLP et al. Coherent control of photocurrent generation in bulk semiconductors. *Phys Rev Lett* **76**, 1703–1706 (1996).
 112. Wang W, Lüpke G, Di Ventra M et al. Coupled electron-hole dynamics at the Si-SiO₂ interface. *Phys Rev Lett* **81**, 4224–4227 (1998).
 113. Fomenko V, Hurth C, Ye T et al. Second harmonic generation investigations of charge transfer at chemically-modified semiconductor interfaces. *J Appl Phys* **91**, 4394–4398 (2002).
 114. Glinka YD, Wang W, Singh SK et al. Characterization of charge-carrier dynamics in thin oxide layers on silicon by second harmonic generation. *Phys Rev B* **65**, 193103 (2002).
 115. Mitchell SA, Ward TR, Wayner DDM et al. Charge trapping at

- chemically modified Si(111) surfaces studied by optical second harmonic generation. *J Phys Chem B* **106**, 9873–9882 (2002).
116. Fomenko V, Borguet E. Combined electron-hole dynamics at UV-irradiated ultrathin Si-SiO₂ interfaces probed by second harmonic generation. *Phys Rev B* **68**, 081301(R) (2003).
117. Scheidt T, Rohwer EG, Von Bergmann HM et al. Charge-carrier dynamics and trap generation in native Si/SiO₂ interfaces probed by optical second-harmonic generation. *Phys Rev B* **69**, 165314 (2004).
118. Scheidt T, Rohwer EG, Neethling P et al. Ionization and shielding of interface states in native p⁺-Si/SiO₂ probed by electric field induced second harmonic generation. *J Appl Phys* **104**, 083712 (2008).
119. Fiore JL, Fomenko VV, Bodladi D et al. Second harmonic generation probing of dopant type and density at the Si/SiO₂ interface. *Appl Phys Lett* **98**, 041905 (2011).
120. Zhang B, Stehr JE, Chen PP et al. Anomalous strong second-harmonic generation in GaAs nanowires via crystal-structure engineering. *Adv Funct Mater* **31**, 2104671 (2021).
121. Fomenko V, Lami JF, Borguet E. Nonquadratic second-harmonic generation from semiconductor-oxide interfaces. *Phys Rev B* **63**, 121316(R) (2001).
122. Giugni A, Torre B, Toma A et al. Hot-electron nanoscopy using adiabatic compression of surface plasmons. *Nat Nanotechnol* **8**, 845–852 (2013).
123. Sun YL, Larin A, Mozharov et al. All-optical generation of static electric field in a single metal-semiconductor nanoantenna. *Light Sci Appl* **12**, 237 (2023).
124. Tagliabue G, DuChene JS, Abdellah M et al. Ultrafast hot-hole injection modifies hot-electron dynamics in Au/p-GaN heterostructures. *Nat Mater* **19**, 1312–1318 (2020).
125. Devižis A, Serbenta A, Meerholz K et al. Ultrafast dynamics of carrier mobility in a conjugated polymer probed at molecular and microscopic length scales. *Phys Rev Lett* **103**, 027404 (2009).
126. Clavero C. Plasmon-induced hot-electron generation at nanoparticle/metal-oxide interfaces for photovoltaic and photocatalytic devices. *Nat Photonics* **8**, 95–103 (2014).
127. Besteiro LV, Kong XT, Wang ZM et al. Understanding hot-electron generation and plasmon relaxation in metal nanocrystals: quantum and classical mechanisms. *ACS Photonics* **4**, 2759–2781 (2017).
128. Mascaretti L, Naldoni A. Hot electron and thermal effects in plasmonic photocatalysis. *J Appl Phys* **128**, 041101 (2020).
129. Khurgin J, Bykov AY, Zayats AV. Hot-electron dynamics in plasmonic nanostructures: fundamentals, applications and overlooked aspects. *eLight* **4**, 15 (2024).
130. Sundararaman R, Narang P, Jermyn AS et al. Theoretical predictions for hot-carrier generation from surface plasmon decay. *Nat Commun* **5**, 5788 (2014).
131. Brongersma ML, Halas NJ, Nordlander P. Plasmon-induced hot carrier science and technology. *Nat Nanotechnol* **10**, 25–34 (2015).
132. Zheng BY, Zhao HQ, Manjavacas A et al. Distinguishing between plasmon-induced and photoexcited carriers in a device geometry. *Nat Commun* **6**, 7797 (2015).
133. Wen XL, Xu WG, Zhao WJ et al. Plasmonic hot carriers-controlled second harmonic generation in WSe₂ bilayers. *Nano Lett* **18**, 1686–1692 (2018).
134. Taghinejad M, Xu ZH, Lee KT et al. Transient second-order nonlinear media: breaking the spatial symmetry in the time domain via hot-electron transfer. *Phys Rev Lett* **124**, 013901 (2020).
135. Billat A, Grassani D, Pfeiffer MHP et al. Large second harmonic generation enhancement in Si₃N₄ waveguides by all-optically induced quasi-phase-matching. *Nat Commun* **8**, 1016 (2017).
136. Hickstein DD, Carlson DR, Mundoor H et al. Self-organized nonlinear gratings for ultrafast nanophotonics. *Nat Photonics* **13**, 494–499 (2019).
137. Lu XY, Moille G, Rao A et al. Efficient photoinduced second-harmonic generation in silicon nitride photonics. *Nat Photonics* **15**, 131–136 (2021).
138. Nitiss E, Hu JQ, Stroganov A et al. Optically reconfigurable quasi-phase-matching in silicon nitride microresonators. *Nat Photonics* **16**, 134–141 (2022).
139. Anderson DZ, Mizrahi V, Sipe JE. Model for second-harmonic generation in glass optical fibers based on asymmetric photoelectron emission from defect sites. *Opt Lett* **16**, 796–798 (1991).
140. Stolen RH, Tom HWK. Self-organized phase-matched harmonic generation in optical fibers. *Opt Lett* **12**, 585–587 (1987).
141. Nitiss E, Liu TY, Grassani D et al. Formation rules and dynamics of photoinduced χ⁽²⁾ gratings in silicon nitride waveguides. *ACS Photonics* **7**, 147–153 (2020).
142. Porcel MAG, Mak J, Taballione C et al. Photo-induced second-order nonlinearity in stoichiometric silicon nitride waveguides. *Opt Express* **25**, 33143–33159 (2017).
143. Yakar O, Nitiss E, Hu JQ et al. Generalized coherent photogalvanic effect in coherently seeded waveguides. *Laser Photonics Rev* **16**, 2200294 (2022).
144. Haché A, Kostoulas Y, Atanasov R et al. Observation of coherently controlled photocurrent in Unbiased, Bulk GaAs. *Phys Rev Lett* **78**, 306–309 (1997).
145. Margulis W, Laurell F, Lesche B. Imaging the nonlinear grating in frequency-doubling fibres. *Nature* **378**, 699–701 (1995).
146. Nitiss E, Zabelich B, Yakar O et al. Broadband quasi-phase-matching in dispersion-engineered all-optically poled silicon nitride waveguides. *Photonics Res* **8**, 1475–1483 (2020).
147. Qian SQ, Snow JB, Tzeng HM et al. Lasing droplets: highlighting the liquid-air interface by laser emission. *Science* **231**, 486–488 (1986).
148. Braginsky VB, Gorodetsky ML, Ilchenko VS. Quality-factor and nonlinear properties of optical whispering-gallery modes. *Phys Lett A* **137**, 393–397 (1989).
149. Lin HB, Campillo AJ. Cw nonlinear optics in droplet microcavities displaying enhanced gain. *Phys Rev Lett* **73**, 2440–2443 (1994).
150. Carmon T, Vahala KJ. Visible continuous emission from a silica microphotonic device by third-harmonic generation. *Nat Phys* **3**, 430–435 (2007).
151. Furst JU, Strekalov DV, Elser D et al. Naturally phase-matched second-harmonic generation in a whispering-gallery-mode resonator. *Phys Rev Lett* **104**, 153901 (2010).
152. Kuo PS, Bravo-Abad J, Solomon GS. Second-harmonic generation using -quasi-phase-matching in a GaAs whispering-gallery-mode microcavity. *Nat Commun* **5**, 3109 (2014).
153. Breunig I. Three-wave mixing in whispering gallery resonators. *Laser Photonics Rev* **10**, 569–587 (2016).
154. Xue XX, Leo F, Xuan Y et al. Second-harmonic-assisted four-wave mixing in chip-based microresonator frequency comb generation. *Light Sci Appl* **6**, e16253 (2016).
155. Zhang XY, Cao QT, Wang Z et al. Symmetry-breaking-induced nonlinear optics at a microcavity surface. *Nat Photonics* **13**, 21–24 (2019).
156. Hu JQ, Nitiss E, He JJ et al. Photo-induced cascaded harmonic and comb generation in silicon nitride microresonators. *Sci Adv* **8**, eadd8252 (2022).
157. Zhou J, Hu JQ, Clementi M et al. Self-organized spatiotemporal quasi-phase-matching in microresonators. *Nat Commun* **16**, 4083 (2025).
158. Gladyshev S, Frizyuk K, Bogdanov A. Symmetry analysis and multipole classification of eigenmodes in electromagnetic resonators for engineering their optical properties. *Phys Rev B* **102**, 075103 (2020).
159. Rybin MV, Koshelev KL, Sadrieva ZF et al. High-Q supercavity

- modes in subwavelength dielectric resonators. *Phys Rev Lett* **119**, 243901 (2017).
160. Bogdanov AA, Koshelev KL, Kapitanova PV et al. Bound states in the continuum and Fano resonances in the strong mode coupling regime. *Adv Photonics* **1**, 016001 (2019).
 161. Zhang F, Solodovchenko NS, Fan HK et al. Non-Hermitian singularities in scattering spectra of Mie resonators. *Sci Adv* **11**, eadr9183 (2025).
 162. Toftul I, Tonkaev P, Koshelev K et al. Chiral dichroism in resonant metasurfaces with monoclinic lattices. *Phys Rev Lett* **133**, 216901 (2024).
 163. Hsu CW, Zhen B, Lee J et al. Observation of trapped light within the radiation continuum. *Nature* **499**, 188–191 (2013).
 164. Zhen B, Hsu CW, Lu L et al. Topological nature of optical bound states in the continuum. *Phys Rev Lett* **113**, 257401 (2014).
 165. Hsu CW, Zhen B, Stone AD et al. Bound states in the continuum. *Nat Rev Mater* **1**, 16048 (2016).
 166. Koshelev K, Lepeshov S, Liu MK et al. Asymmetric metasurfaces with high-Q resonances governed by bound states in the continuum. *Phys Rev Lett* **121**, 193903 (2018).
 167. Yu NF, Genevet P, Kats MA et al. Light propagation with phase discontinuities: generalized laws of reflection and refraction. *Science* **334**, 333–337 (2011).
 168. Meinzer N, Barnes WL, Hooper IR. Plasmonic meta-atoms and metasurfaces. *Nat Photonics* **8**, 889–898 (2014).
 169. Rahimi E, Gordon R. Nonlinear plasmonic metasurfaces. *Adv Opt Mater* **6**, 1800274 (2018).
 170. Wang BQ, Yu P, Wang WH et al. High-Q plasmonic resonances: fundamentals and applications. *Adv Opt Mater* **9**, 2001520 (2021).
 171. Zhao Y, Yang YM and Sun HB. Nonlinear meta-optics towards applications. *PhotonIX* **2**, 3 (2021).
 172. Grinblat G. Nonlinear dielectric nanoantennas and metasurfaces: frequency conversion and wavefront control. *ACS Photonics* **8**, 3406–3432 (2021).
 173. Krasnok A, Tymchenko M, Alù A. Nonlinear metasurfaces: a paradigm shift in nonlinear optics. *Mater Today* **21**, 8–21 (2018).
 174. Li GX, Zhang S, Zentgraf T. Nonlinear photonic metasurfaces. *Nat Rev Mater* **2**, 17010 (2017).
 175. Lapine M, Shadrivov IV, Kivshar YS. *Colloquium: nonlinear metamaterials*. *Rev Mod Phys* **86**, 1093–1123 (2014).
 176. Huang LJ, Xu L, Powell DA et al. Resonant leaky modes in all-dielectric metasystems: fundamentals and applications. *Phys Rep* **1008**, 1–66 (2023).
 177. Koshelev K, Tang YT, Li KF et al. Nonlinear metasurfaces governed by bound states in the continuum. *ACS Photonics* **6**, 1639–1644 (2019).
 178. Cai WS, Vasudev AP, Brongersma ML. Electrically controlled nonlinear generation of light with plasmonics. *Science* **333**, 1720–1723 (2011).
 179. Kang L, Cui YH, Lan SF et al. Electrifying photonic metamaterials for tunable nonlinear optics. *Nat Commun* **5**, 4680 (2014).
 180. Lan SF, Rodrigues S, Cui YH et al. Electrically tunable harmonic generation of light from plasmonic structures in electrolytes. *Nano Lett* **16**, 5074–5079 (2016).
 181. Liu TJ, Xu RY, Yu P et al. Multipole and multimode engineering in mie resonance-based metastructures. *Nanophotonics* **9**, 1115–1137 (2020).
 182. Minovich AE, Miroshnichenko AE, Bykov AY et al. Functional and nonlinear optical metasurfaces. *Laser Photonics Rev* **9**, 195–213 (2015).
 183. Lee KT, Taghinejad M, Yan JH et al. Electrically biased silicon metasurfaces with magnetic mie resonance for tunable harmonic generation of light. *ACS Photonics* **6**, 2663–2670 (2019).
 184. Khurgin JB. Current induced second harmonic generation in semiconductors. *Appl Phys Lett* **67**, 1113–1115 (1995).
 185. Wu SF, Mao L, Jones AM et al. Quantum-enhanced tunable second-order optical nonlinearity in bilayer graphene. *Nano Lett* **12**, 2032–2036 (2012).
 186. Aktsipetrov OA, Bessonov VO, Fedyanin AA et al. DC-induced generation of the reflected second harmonic in silicon. *JETP Lett* **89**, 58–62 (2009).
 187. An YQ, Nelson F, Lee JU et al. Enhanced optical second-harmonic generation from the current-biased graphene/SiO₂/Si(001) structure. *Nano Lett* **13**, 2104–2109 (2013).
 188. Costa L, Betz M, Spasenović M et al. All-optical injection of ballistic electrical currents in unbiased silicon. *Nat Phys* **3**, 632–635 (2007).
 189. Werake LK, Zhao H. Observation of second-harmonic generation induced by pure spin currents. *Nat Phys* **6**, 875–878 (2010).
 190. Lee J, Nookala N, Gomez-Diaz JS et al. Ultrathin second-harmonic metasurfaces with record-high nonlinear optical response. *Adv Opt Mater* **4**, 664–670 (2016).
 191. Krakofsky JH, Sarma R, Brener I et al. Flat nonlinear optics with intersubband polaritonic metasurfaces. *Nanophotonics* **14**, 3709–3721 (2025).
 192. Capasso F, Paiella R, Martini R et al. Quantum cascade lasers: ultrahigh-speed operation, optical wireless communication, narrow linewidth, and far-infrared emission. *IEEE J Quant Electron* **38**, 511–532 (2002).
 193. Gmachl C, Belyanin A, Sivco DL et al. Optimized second-harmonic generation in quantum cascade lasers. *IEEE J Quant Electron* **39**, 1345–1355 (2003).
 194. Lee J, Tymchenko M, Argyropoulos C et al. Giant nonlinear response from plasmonic metasurfaces coupled to intersubband transitions. *Nature* **511**, 65–69 (2014).
 195. Rosencher E, Fiore A, Vinter B et al. Quantum engineering of optical nonlinearities. *Science* **271**, 168–173 (1996).
 196. Belkin MA, Capasso F, Belyanin A et al. Terahertz quantum-cascade-laser source based on intracavity difference-frequency generation. *Nat Photonics* **1**, 288–292 (2007).
 197. Vijayraghavan K, Jiang YF, Jang M et al. Broadly tunable terahertz generation in mid-infrared quantum cascade lasers. *Nat Commun* **4**, 2021 (2013).
 198. Sarma R, Xu JM, de Ceglia D et al. An all-dielectric polaritonic metasurface with a giant nonlinear optical response. *Nano Lett* **22**, 896–903 (2022).
 199. Barbet G, Qiang B, Jin YH et al. Epsilon-near-zero enhancement of nonlinear responses from intersubband transitions in the mid-infrared. *Adv Opt Mater* **11**, 2202786 (2023).
 200. Nefedkin N, Mekawy A, Krakofsky J et al. Overcoming intensity saturation in nonlinear multiple-quantum-well metasurfaces for high-efficiency frequency upconversion. *Adv Mater* **35**, 2106902 (2023).
 201. Kim D, Yu J, Boehm G et al. Efficient second-harmonic generation from dielectric inter-subband polaritonic metasurfaces coupled to lattice resonance. *Nano Lett* **23**, 9003–9010 (2023).
 202. Chen CF, Qian HL, Liu ZW. Electrically tunable strong optical nonlinearity in near-infrared by coupled metallic quantum wells. *Adv Opt Mater* **12**, 2302176 (2024).
 203. Jin W, Yang QF, Chang L et al. Hertz-linewidth semiconductor lasers using CMOS-ready ultra-high-Q microresonators. *Nat Photonics* **15**, 346–353 (2021).
 204. Corato-Zanarella M, Gil-Molina A, Ji XC et al. Widely tunable and narrow-linewidth chip-scale lasers from near-ultraviolet to near-infrared wavelengths. *Nat Photonics* **17**, 157–164 (2023).
 205. Xiang C, Liu JQ, Guo J et al. Laser soliton microcombs heterogeneously integrated on silicon. *Science* **373**, 99–103 (2021).
 206. Spencer DT, Drake T, Briles TC et al. An optical-frequency

- synthesizer using integrated photonics. *Nature* **557**, 81–85 (2018).
207. Zhang XG, Zhou ZX, Guo YJ et al. High-coherence parallelization in integrated photonics. *Nat Commun* **15**, 7892 (2024).
 208. Zhang XP, Zhang XG, Chen YJ et al. Microcomb-synchronized optoelectronics. *Nat Electron* **8**, 322–330 (2025).
 209. Baumgartner R, Byer R. Optical parametric amplification. *IEEE J Quant Electron* **15**, 432–444 (1979).
 210. Heydari D, Cătuneanu M, Ng E et al. Degenerate optical parametric amplification in CMOS silicon. *Optica* **10**, 430–437 (2023).
 211. Clementi M, Zatti L, Zhou J et al. Ultrabroadband milliwatt-level resonant frequency doubling on a chip. *Nat Commun* **16**, 6164 (2025).
 212. Clementi M, Nitiss E, Liu JQ et al. A chip-scale second-harmonic source via self-injection-locked all-optical poling. *Light Sci Appl* **12**, 296 (2023).
 213. Li BH, Yuan ZQ, Williams J et al. Down-converted photon pairs in a high-Q silicon nitride microresonator. *Nature* **639**, 922–927 (2025).
 214. Manaka T, Lim E, Tamura R et al. Direct imaging of carrier motion in organic transistors by optical second-harmonic generation. *Nat Photonics* **1**, 581–584 (2007).
 215. Manaka T, Iwamoto M. Optical second-harmonic generation measurement for probing organic device operation. *Light Sci Appl* **5**, e16040 (2016).
 216. Lee K, Park J, Kang BJ et al. Electrically controllable terahertz second-harmonic generation in GaAs. *Adv Opt Mater* **8**, 2000359 (2020).
 217. Manaka T, Lim E, Tamura R et al. Modulation in optical second harmonic generation signal from channel of pentacene field effect transistors during device operation. *Appl Phys Lett* **87**, 222107 (2005).
 218. Lim E, Manaka T, Tamura R et al. Maxwell-wagner model analysis for the capacitance-voltage characteristics of pentacene field effect transistor. *Jpn J Appl Phys* **45**, 3712–3716 (2006).
 219. Tamura R, Lim E, Manaka T et al. Analysis of pentacene field effect transistor as a Maxwell-Wagner effect element. *J Appl Phys* **100**, 114515 (2006).
 220. Xiao M, Martin I, Yablonovitch E et al. Electrical detection of the spin resonance of a single electron in a silicon field-effect transistor. *Nature* **430**, 435–439 (2004).
 221. Adinolfi V, Sargent EH. Photovoltage field-effect transistors. *Nature* **542**, 324–327 (2017).
 222. Horowitz G. Organic field-effect transistors. *Adv Mater* **10**, 365–377 (1998).
 223. Taguchi D, Weis M, Manaka T et al. Probing of carrier behavior in organic electroluminescent diode using electric field induced optical second-harmonic generation measurement. *Appl Phys Lett* **95**, 263310 (2009).
 224. Weis M, Manaka T, Iwamoto M. Origin of electric field distribution in organic field-effect transistor: experiment and analysis. *J Appl Phys* **105**, 024505 (2009).
 225. Taguchi D, Inoue S, Zhang L et al. Analysis of organic light-emitting diode as a maxwell-wagner effect element by time-resolved optical second harmonic generation measurement. *J Phys Chem Lett* **1**, 803–807 (2010).
 226. Xu YJ, Liu N, Lin Y et al. Enhancements of electric field and afterglow of non-equilibrium plasma by Pb(Zr_xTi_{1-x})O₃ ferroelectric electrode. *Nat Commun* **15**, 3092 (2024).
 227. Vithanage DA, Devižis A, Abramavičius V et al. Visualizing charge separation in bulk heterojunction organic solar cells. *Nat Commun* **4**, 2334 (2013).
 228. Tisdale WA, Williams KJ, Timp BA et al. Hot-electron transfer from semiconductor nanocrystals. *Science* **328**, 1543–1547 (2010).
 229. Nelson J. *The Physics of Solar Cells* (World Scientific, London, 2003).
 230. Yi JC, Zhang GY, Yu H et al. Advantages, challenges and molecular design of different material types used in organic solar cells. *Nat Rev Mater* **9**, 46–62 (2024).
 231. Melianas A, Pranculis V, Devižis A et al. Dispersion-dominated photocurrent in polymer: fullerene solar cells. *Advanced Funct Mater* **24**, 4507–4514 (2014).
 232. Jailaubekov AE, Willard AP, Tritsch JR et al. Hot charge-transfer excitons set the time limit for charge separation at donor/acceptor interfaces in organic photovoltaics. *Nat Mater* **12**, 66–73 (2013).
 233. Alivisatos AP. Semiconductor clusters, nanocrystals, and quantum dots. *Science* **271**, 933–937 (1996).
 234. Williams KJ, Nelson CA, Yan X et al. Hot electron injection from graphene quantum dots to TiO₂. *ACS Nano* **7**, 1388–1394 (2013).
 235. Lee YS. *Principles of Terahertz Science and Technology* (Springer, New York, 2009).
 236. Fan KB, Hwang HY, Liu MK et al. Nonlinear terahertz metamaterials via field-enhanced carrier dynamics in GaAs. *Phys Rev Lett* **110**, 217404 (2013).
 237. Chen F, Goodfellow J, Liu S et al. Ultrafast terahertz gating of the polarization and giant nonlinear optical response in BiFeO₃ thin films. *Adv Mater* **27**, 6371–6375 (2015).
 238. Bässler H, Köhler A. "Hot or cold": how do charge transfer states at the donor–acceptor interface of an organic solar cell dissociate. *Phys Chem Chem Phys* **17**, 28451–28462 (2015).
 239. Goswami A, Kim AS, Cai WS. Exploring the synergy between hot-electron dynamics and active plasmonics: a perspective. *J Appl Phys* **136**, 100901 (2024).

Acknowledgements

The authors are thankful to Yuri Kivshar, Mikhail Lapine and Wenshan Cai for the fruitful discussions. This research was supported by Priority 2030 Federal Academic Leadership Program. Program. A.P. acknowledges BASIS Foundation.

Author contributions

All authors commented on the manuscript.

Competing interests

The authors declare no competing financial interests.



Open Access This article is licensed under a Creative Commons Attribution 4.0 International License, which permits use, sharing, adaptation, distribution and reproduction in any medium or format, as long as you give appropriate credit to the original author(s) and the source, provide a link to the Creative Commons license, and indicate if changes were made. To view a copy of this license, visit <http://creativecommons.org/licenses/by/4.0/>

©The Author(s) 2026.

Published by Editorial Office of *Opto-Electronic Advance*, Institute of Optics and Electronics, Chinese Academy of Sciences.

